Available online at www.sciencedirect.com
SCIENCE DIRECT
International Journal of Heat and Mass Transfer 49 (2006) 4305–4324
International Journal of HEAT and MASS TRANSFER
www.elsevier.com/locate/ijhmt

Turbulent transport of passive scalar behind line sources in an unstably stratified open channel flow

Chun-Ho Liu [a,*], Dennis Y.C. Leung [b]

[a] Department of Building and Real Estate, The Hong Kong Polytechnic University, Hung Hom, Kowloon, Hong Kong
[b] Department of Mechanical Engineering, The University of Hong Kong, Hong Kong

Received 14 February 2005; received in revised form 8 May 2006

Abstract

This study employs a direct numerical simulation (DNS) technique to study the flow, turbulence structure, and passive scalar plume transport behind line sources in an unstably stratified open channel flow. The scalar transport behaviors for five emission heights ($z_s = 0$, $0.25H$, $0.5H$, $0.75H$, and H, where H is the channel height) at a Reynolds number of 3000, a Prandtl number and a Schmidt number of 0.72, and a Richardson number of -0.2 are investigated. The vertically meandering mean plume heights and dispersion coefficients calculated by the current DNS model agree well with laboratory results and field measurements in literature. It is found that the plume meandering is due to the movement of the positive and negative vertical turbulent scalar fluxes above and below the mean plume heights, respectively. These findings help explaining the plume meandering mechanism in the unstably stratified atmospheric boundary layer.

Keywords: Open channel flow; Atmospheric boundary layer (ABL); Unstable stratification; Line sources; Vertical plume meandering; Direct numerical simulation (DNS)

1. Introduction

Transport of passive and inert[1] scalar in turbulent flow exhibits a broad range of spatial and temporal scales governed by the characteristics of fluid turbulence. The transport is further complicated by the existence of temperature stratification. Heating at the bottom leads to buoyancy opposite to the gravitational force and increases turbulence kinetic energy (TKE). This configuration of turbulent boundary layer (TBL), also known as unstably stratified or convective boundary layer (CBL), is commonly observed in the daytime atmospheric boundary layer (ABL). The fluid motions in a CBL exhibit a coherent structure of circulation consisting of updrafts and downdrafts [1] that tremendously affects the plume behaviors for scalar emitted continuously from point or line sources. Unlike the cases in neutral stratification, remarkable plume meandering in the form of ascending and descending scalar trajectories is observed in CBLs. For example, maximum ground-level concentration from elevated sources, such as chimneys, is often encountered in a day-time CBL with light wind. Under this circumstance, conventional Gaussian plume models no longer calculate the scalar transport accurately. In fact, our understanding on the mechanism of scalar transport in CBLs is limited.

Willis and Deardorff [2] constructed a laboratory convective water tank to model the turbulence structure in CBLs. The experiment was further developed to investigate the transport of scalar emitted at different heights [3–5]. The characteristic scalar transport behaviors (the plume ascent and descent) in a CBL were then established together with the convective mixed-layer scaling velocity $w_* = (g/\Theta_0\langle w''\theta''\rangle|_{z=0} z_i)^{1/3}$ [6]. Recently, Weil et al. [7] utilized a laboratory convective water tank to study the

* Corresponding author. Tel.: +852 2766 5877; fax: +852 2764 5131.
E-mail address: liuchunho@graduate.hku.hk (C.-H. Liu).

[1] In this paper, passive means that the physical properties of the scalar are exactly equal to those of the carrier fluid and the scalar does not affect the fluid motions. Inert means that the scalar is not involved in any chemical reaction.

0017-9310/$ - see front matter © 2006 Elsevier Ltd. All rights reserved.
doi:10.1016/j.ijheatmasstransfer.2006.05.026

Nomenclature

C	the source strength and the reference scalar mixing ratio
c	scalar mixing ratio
g	gravitational acceleration
H	the channel height and the reference length scale
L_{x_i}	domain extents ($i = 1$, 2, and 3 in the streamwise (L_x), spanwise (L_y), and vertical (L_z) directions, respectively)
N_{x_i}	number of elements ($i = 1$, 2, and 3 in the streamwise (N_x), spanwise (N_y), and vertical (N_x) directions, respectively)
p	kinematic pressure
Pr	Prandtl number $= \nu/\alpha$
$R_{\phi\psi}$	correlation coefficient between ϕ and ψ defined in Eq. (8)
Re	Reynolds number $= UH/\nu$
Re_τ	Reynolds number based on wall variables $= u_\tau H/\nu$
Ri	Richardson number $= -g(H/\Theta_0)(\Delta\Theta/U^2)$
Sc	Schmidt number $= \nu/\kappa$
T	the reference time scale $= H/U$
t	time
U	the mean flow speed at the top of the channel and the reference velocity scale
u_i	velocity components ($i = 1$, 2, and 3 are the velocity components in the streamwise (u), spanwise (v), and vertical (w) directions, respectively)
u_τ	friction velocity
w_*	convective mixed-layer scaling velocity $= (g/\Theta_0\langle w''\theta''\rangle\|_{z=0})^{1/3}$
$\theta''w''$	vertical heat flux
X^*	streamwise distance made dimensionless by the convective mixed-layer scaling velocity $= (w^*/U)(x/H)$
x_i	Cartesian coordinates ($i = 1$, 2, and 3 for the streamwise x, spanwise y, and vertical z directions, respectively)
$\bar{z}(x)$	mean plume height defined in Eq. (6)
z_i	height of the turbulent boundary layer
z_s	scalar emission height
α	thermal diffusivity
Δt	time step increment
$\Delta\Theta$	the mean temperature difference across the channel and the reference temperature scale
Δx_i	mesh spacing ($i = 1$, 2, and 3 for the streamwise Δx, spanwise Δy, and vertical Δz directions, respectively)
δ_{ij}	Kronecker symbol
κ	mass diffusivity
ν	kinematic viscosity
$\sigma_z(x)$	vertical scalar dispersion coefficient defined in Eq. (7)
Θ_0	reference temperature
θ	temperature
$\langle\,\rangle$	statistical mean, spatial (homogeneous directions) and temporal average

Superscripts

$''$	deviation from the statistical mean $\phi'' = \phi - \langle\phi\rangle$
$+$	parameters expressed in wall unit

transport behavior of passive scalar behind point sources in which a plume meandering was observed. Apart from water tank experiments, ascents and descents of scalar trajectories were observed in a modeled CBL in a thermally stratified wind tunnel [8]. These experiments have built up our basic knowledge of characteristic scalar transport in CBLs and have speculated the reliability of conventional Gaussian plume models. Hence, theoretical analysis by mathematical modeling is deemed for better understanding on the detailed scalar transport mechanism underneath.

Second-order closure turbulence models, which parameterize the subgrid-scale processes by single-length-scale models, are commonly adopted in studies of turbulent transport. Though all the processes in the spanwise direction were neglected, the two-dimensional (2D) studies by Sun and Chang [9] and Pai and Tsang [10] calculated the plume meandering for scalar emitted at different heights in CBLs. The three-dimensional (3D) study by Liu and Leung [11] further confirmed this unique plume meandering.

The second-order closure turbulence models assume single-length-scale subgrid-scale processes that can rarely model the broad spectrum of scales in turbulent transport to good accuracy. The inaccuracy is particularly considerable when the turbulence is due to buoyancy and mechanical shear simultaneously. Large-eddy simulation (LES) calculates explicitly most of the actual transport of momentum and mass while the remaining small amount of Reynolds stresses and scalar fluxes are modeled by subgrid-scale parameterizations. It is thus less sensitive to the inaccuracy of parameterizations. Numerous LES studies have been conducted to investigate the turbulence structures in CBLs [1,12–15]. Based on LES-calculated flow fields, Lagrangian stochastic particle models have been employed to investigate the scalar plume transport in CBLs [16–18] in which the findings agreed well with measurements. Eulerian models have also played important roles to investigate the scalar plume transport behaviors in different buoyancy- and shear-driven CBLs using LES [19,20]. These mathematical modeling studies, using both Lagrangian and Eulerian approaches, have calculated the unique plume behaviors and elucidate the plume transport mechanisms in CBLs.

Although LES calculates explicitly most of the large energy-carrying scales and models only the small subgrid scales, no agreed subgrid-scale parameterization has been reached yet. Indeed, the differences among those subgrid-scale models become significant when the subgrid-scale kinetic energy and the inter-scale energy transfer are investigated [21]. Numerous subgrid-scale models, including Smagorinsky eddy-viscosity model [22], one-equation eddy-viscosity model [23], dynamic model [24], dynamic mixed model [25], and dynamic localization model [26], just name a few, are available in literature. On the other hand, direct numerical simulation (DNS), which calculates explicitly all the significant energy-carrying scales, provides a more accurate solution to the detailed transport processes in fluid turbulence. However, because of the highly refined spatio-temporal resolution required, DNS is restricted to flow at small Reynolds numbers. It is thus limited to engineering-scale and is hardly extended to the full-scale ABL. Nonetheless, reduced-scale DNS models are good representations of the ABL physics that help explain the actual transport processes and mechanisms. DNS of horizontally homogeneous scalar transport inside a turbulent channel was conducted by Kim and Moin [27] and constructed the basic correlations between fluid and scalar motions. The characteristic structure and development of the scalar wake behind passive scalar line sources placed perpendicular to the flow in homogeneous turbulence were investigated by Li and Bilger [28] and Livescu et al. [29]. The mean and root-mean-square (RMS) statistics agreed well with those obtained from experiments.

In the light of the uncertainties of subgrid-scale parameterizations in LES, this study aims at using a DNS model to explain the transport behaviors of passive scalar plume behind line sources in an unstably stratified open channel flow. Because of the refined spatial resolution required, the current DNS calculation is limited to an engineering scale at a small Reynolds number that utilizes an open channel to represent the ABL. The effects of temperature stratification on turbulence, scalar mixing ratio, scalar fluxes, correlation coefficients, scalar mixing ratio budget, and instantaneous fields are studied to improve our understanding on the behaviors and mechanism of scalar plume transport, as well as to supplement previous findings from mathematical modeling, laboratory experiments, and field measurements.

2. Mathematical model

Incompressible flow of Boussinesq fluid is considered in the current DNS model in which the governing equations include the following:

(i) conservation of momentum equation:

$$\frac{\partial u_i}{\partial t}+\frac{\partial}{\partial x_j}u_iu_j=-\frac{\partial p}{\partial x_i}+\frac{1}{Re}\frac{\partial^2 u_i}{\partial x_j\partial x_j}-Ri(\theta-\Theta_0)\delta_{i3}, \tag{1}$$

(ii) continuity equation:

$$\frac{\partial u_i}{\partial x_i}=0, \tag{2}$$

(iii) conservation of energy equation:

$$\frac{\partial \theta}{\partial t}+\frac{\partial}{\partial x_i}\theta u_i=\frac{1}{RePr}\frac{\partial^2\theta}{\partial x_i\partial x_i}. \tag{3}$$

The above equations are expressed in tensor notation and the usual summation convention on repeated indices (i and j) is employed. All variables in the equations are appropriately made dimensionless by the channel height H, the mean flow speed at the top of channel U, and the mean temperature difference across the channel $\Delta\Theta$. The dimensionless parameters used thus include the Reynolds number Re, the Prandtl number Pr, and the Richardson number Ri. The Ri is used to account for the relative contribution from buoyancy and shear that is negative in unstable stratification. The (passive and inert) scalar transport is calculated by

(iv) mass conservation equation:

$$\frac{\partial c}{\partial t}+\frac{\partial}{\partial x_i}cu_i=\frac{1}{ReSc}\frac{\partial^2 c}{\partial x_i\partial x_i}. \tag{4}$$

It is made dimensionless by the scalar source strength C with Re and the Schmidt number Sc to be the dimensionless parameters.

3. Computational information

3.1. Numerical methodology

The governing equations (1)–(4) are solved by a 3D finite element method (FEM). The implicit dependence of velocity and pressure in incompressible flow is decoupled by a second-order accurate fractional-step method. The Galerkin method is used to construct the weighted residual formulation of the mathematical model. The velocity, pressure, temperature, and scalar mixing ratio are approximated by the same trilinear interpolating polynomials based on brick elements. The nonlinear advection terms are solved explicitly by a third-order accurate Runge–Kutta scheme while the linear diffusion terms are solved implicitly by a second-order accurate Crank–Nicolson scheme. The buoyancy term in the momentum equation is solved explicitly by a first-order accurate Euler scheme. The aforementioned mathematical procedure leads to several systems of linear equations which are solved by the Conjugate Gradient iteration with Jacobian preconditioning [30]. The detailed numerical methodology is discussed elsewhere [31,32]. The DNS FEM code is parallelized by domain decomposition for data structure together with data parallelism for matrix assemblies and operations [33]. The computation was undertaken on Linux PC clusters consisting of 16 CPUs whose parallel performance is discussed by Liu et al. [34]. An *in prior* model validation has been conducted by simulating turbulent transport in

a plane Couette flow [35] in addition to the model validation presented later in this paper.

3.2. Computational domain and boundary conditions

In the current DNS calculation, the computational domain is a rectangular channel (Fig. 1) of size $12H$ (streamwise) $\times 4H$ (spanwise) $\times H$ (vertical). Periodic boundary conditions are employed in the horizontal directions for both the flow and temperature calculations. The mean flow is driven by a constant background pressure force in the streamwise direction. In the vertical direction, a non-slip rigid wall boundary condition $u_i = 0$ is assumed at the bottom of the channel while a shear-free boundary condition with no deformation and zero vertical flow ($\partial u/\partial z = \partial v/\partial z = w = 0$) is assumed at the top of the open channel. This configuration is a good representation of a free surface as long as the vertical deformation is negligible compared with the channel height and the Reynolds number is not high [36]. Constant temperature boundary conditions are assumed at the bottom and top of the channel. To simulate unstable stratification, the wall is heated up such that the constant temperature difference across the channel height is $\Delta\Theta$.

Passive scalar is emitted into the open channel through hypothetical line sources placed parallel to the spanwise direction at $x = 0$. Five emission heights, at $z_s/H = 0$, 0.25, 0.5, 0.75, and 1, are considered. Instead of adding source terms into Eq. (4), the scalar sources are simulated in the form of Dirichlet boundary conditions of constant scalar mixing ratio C at the inlet of the open channel. The effects are virtually the same as placing lines of constant temperature in the open channel flow. The upstream inlet is free of scalar while an open boundary condition

$$\frac{\partial c}{\partial t} + u\frac{\partial c}{\partial x} = 0 \tag{5}$$

is assumed at the downstream outlet where the scalar is removed from the channel without obvious distortion or reflection. Unlike the conventional zero-gradient boundary condition, molecular diffusion term is not included in Eq. (5). Indeed, the zero-gradient boundary condition is not appropriate in the current turbulent scalar transport because it would unnecessarily reflect the scalar from the downstream outlet back into the open channel. The scalar transport is assumed to be periodic in the spanwise direction. Zero-gradient boundary conditions for scalar are assumed at the wall and the top of the channel.

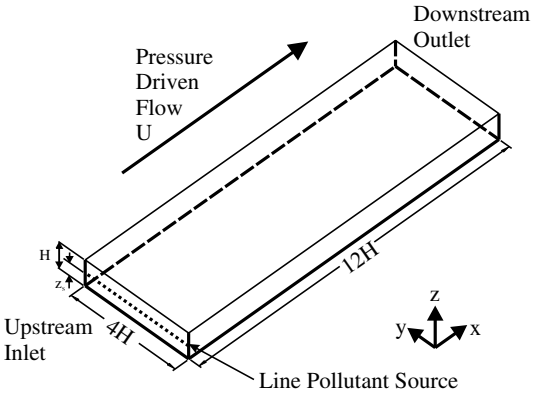

Fig. 1. Schematic diagram of the computational domain for passive scalar transport behind line sources in an unstably stratified open channel flow calculated by the current DNS.

3.3. Simulation parameters

The computational domain is discretized into a mesh consisting of $448 \times 64 \times 96$ ($= 2\,752\,512$) brick finite elements in x, y, and z directions, respectively. The mesh in the spanwise direction is evenly distributed with spacing $\Delta y = 0.0625H$. The vertical mesh spacing Δz is stretched away from the walls, the shear-free boundary, and the scalar sources so as to better resolve the large spatial variation of the calculated variables. The minimum and maximum vertical mesh spacings are $0.004H$ and $0.0244H$, respectively. The streamwise mesh spacing is also stretched away from the scalar sources to capture the rapid plume development in the near field with mesh spacing $\Delta x = 0.011H$ next to the sources. It increases gradually in the streamwise direction with a maximum $\Delta x = 0.065H$ at the downstream outlet. The Reynolds numbers based on wall variables Re_τ ($= u_\tau H/\nu$) and based on global variables Re ($= UH/\nu$) are 180 and 3000, respectively. The Prandtl and Schmidt numbers are set equal to 0.72. The convective velocity scale w_* is 0.2 based on the channel height and the wall heat flux. The ratio of friction velocity to convective velocity scale u_τ/w_* is 0.22. The corresponding Richardson number is -0.2 that represents a CBL with almost calm wind. In the previous convective water channel experiments at higher Reynolds numbers [2–6], the near-wall heat flux is dominated by the turbulent heat flux while the (molecular) heat flux on the wall is difficult to be measured. As a result, the convective mixed-layer scaling velocity is based on the near-wall heat flux. However, our DNS is at a lower Reynolds number and it can calculate the molecular heat flux on the wall. Thus, the DNS-calculated wall-surface molecular heat flux is used to define the convective mixing-layer scaling velocity. The time step increment Δt is 0.01T such that the Courant–Fredrichs–Lewy (CFL) number is less than 0.7. Although the Reynolds number is rather low, the flow is confirmed fully turbulent by previous measurements, LES, and DNS [37]. The current simulation parameters are tabulated in Table 1. The DNS has been carried out for $50T$ for achieving pseudo-steady state. Afterward, the DNS output for another $50T$ was collected for subsequent statistical analyzes that covers about 100 eddy turn-over time.

4. Results and discussion

This study focuses on the transport behaviors of scalar plume in a CBL. The flow field will be discussed briefly

Table 1
Simulation parameters in global and wall units for the current DNS calculation

	Simulation parameters	
	Global units	Wall units
Domain size	$L_x \times L_y \times L_z$ $= 12H \times 4H \times H$	$L_x^+ \times L_y^+ \times L_z^+$ $= 2160 \times 720 \times 180$
Reynolds number	$Re = 3000$	$Re_\tau = 180$
Number of elements	$N_x \times N_y \times N_z$ $= 448 \times 64 \times 96 = 2752512$	
Grid spacing	$0.011H \leqslant \Delta x \leqslant 0.065H$ $\Delta_y = 0.0625H$ $0.004H \leqslant \Delta_z \leqslant 0.0244H$	$1.98 \leqslant \Delta x^+ \leqslant 11.70$ $\Delta y^+ = 11.25$ $0.72 \leqslant \Delta z^+ \leqslant 4.39$
Time step increment	$\Delta t = 0.01T$	$\Delta t^+ = 8.1$
CFL number	$0.11 \leqslant \mathrm{CFL} \leqslant 0.70$	

before going into the detailed scalar transport. In the following discussion, statistical means denoted by parenthesis $\langle\ \rangle$ are spatial (in the homogeneous directions) and temporal average. Hence, the statistical means of flow variables are averaged in both streamwise and spanwise directions while the statistical means of scalar variables are averaged in the spanwise direction only.

4.1. Flow and turbulence properties

The calculated vertical profile of mean streamwise velocity $\langle u\rangle$ grows quickly to its free-stream value U for $z/H \geqslant 0.2$ (Fig. 2a). The relatively constant mean streamwise velocity over most of the channel height is caused by the enhanced turbulent mixing due to the increased vertical Reynolds stress $u''w''$ generated by the buoyancy. Moreover, there is a local minimum of mean streamwise velocity at $z/H = 0.9$. It is mainly due to the sharp change in the RMS streamwise velocity fluctuation together with the free-surface boundary condition imposed at the top of the open channel. Fig. 2b shows the calculated vertical profile of mean temperature $\langle\theta\rangle$ across the channel height. It is asymmetric in which the temperature is relatively constant ($\langle\theta\rangle/\Delta\Theta \approx -0.25$) at the center core of the channel ($0.1 \leqslant z/H \leqslant 0.9$). Analogous to the mean streamwise velocity, the relatively constant mean temperature is due to the increased vertical heat flux $\theta''w''$ at the center core of the channel. The increased Reynolds stress and heat flux signify the enhanced mixing due to buoyancy-driven turbulence in addition to shear-driven turbulence in unstably stratified TBLs. It is worth mentioning that there is a tiny local maximum of mean temperature at $z/H = 0.7$. The formation of this minor peak is mainly due to the buoyancy dominated flow. The hot fluid originated from the lower part of the open channel moves upward rapidly that increases the temperature at $z/H = 0.7$.

The RMS streamwise velocity fluctuation has a near-wall local maximum $\langle u''u''\rangle^{1/2}/U = 0.22$ at $z/H = 0.05$ (Fig. 3a). It decreases with increasing height until $z/H = 0.9$ before increases to $\langle u''u''\rangle^{1/2}/U = 0.16$ at the top of the channel. The unstable stratification greatly increases the RMS spanwise velocity fluctuation $\langle v''v''\rangle^{1/2}$ compared with that in neutral stratification. In particular, the RMS spanwise velocity fluctuation is greater than the streamwise one. It has local maxima of $\langle v''v''\rangle^{1/2}/U = 0.24$ and 0.3 at $z/H = 0.1$ and 1, respectively, together with a local minimum of 0.16 at the channel center. Unlike its streamwise and spanwise counterparts, the RMS vertical velocity fluctuation $\langle w''w''\rangle^{1/2}$ is equal to zero at the top of the channel because of the velocity boundary conditions. Maximum

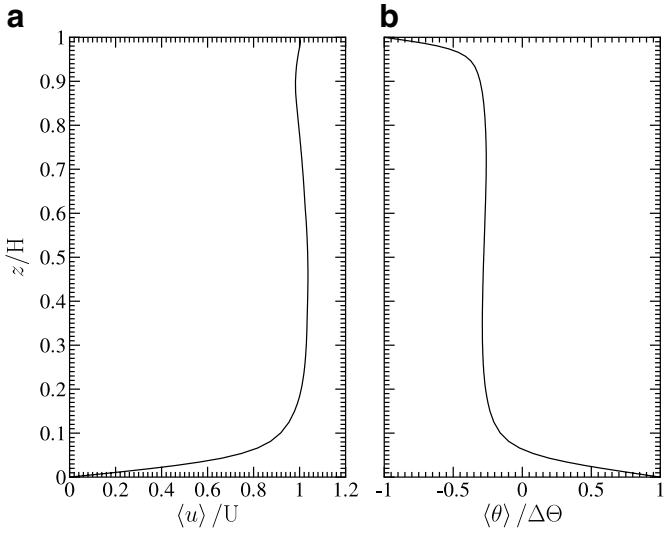

Fig. 2. Vertical profiles of (a) mean flow speed $\langle u\rangle/U$ and (b) mean temperature $\langle\theta\rangle/\Delta\Theta$.

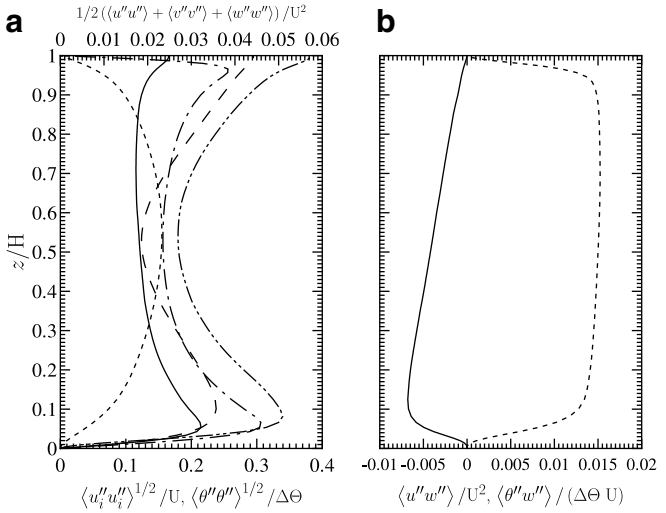

Fig. 3. Vertical profiles of (a) root-mean-square velocity fluctuation (streamwise $\langle u''u''\rangle^{1/2}/U$: —, spanwise $\langle v''v''\rangle^{1/2}/U$: – – –, and vertical $\langle w''w''\rangle^{1/2}/U$: ···), turbulent kinetic energy $1/2\,(\langle u''u''\rangle + \langle v''v''\rangle + \langle w''w''\rangle)$: –··–, and temperature fluctuation $\langle\theta''\theta''\rangle^{1/2}/\Delta\Theta$: –·–, and (b) vertical Reynolds stress $\langle u''w''\rangle/U^2$: — and vertical heat flux $\langle\theta''w''\rangle/(\Delta\Theta U)$: ···.

RMS vertical velocity fluctuation ($\langle w''w''\rangle^{1/2}/U = 0.16$) is observed at the center core of the channel whose location is elevated compared with that in neutral stratification. Also shown in Fig. 3a is the TKE ($=(\langle u''u''\rangle + \langle v''v''\rangle + \langle w''w''\rangle)/(2U^2)$) across the vertical extent of the channel. The redistribution of TKE from the vertical component to the horizontal components near the shear-free boundary of an open channel was confirmed numerically [37] and experimentally [38–40]. The current DNS FEM model also calculates this unique behavior near the shear-free boundary where the RMS vertical velocity fluctuation decreases rapidly while the RMS streamwise and spanwise velocity fluctuations increase (Fig. 3a).

The vertical profile of RMS temperature fluctuation $\langle\theta''\theta''\rangle^{1/2}$ is asymmetric in an unstably stratified TBL (Fig. 3a). Local maxima occur at the near-wall region ($\langle\theta''\theta''\rangle^{1/2}/\Delta\Theta = 0.31$ at $z/H = 0.06$) and near the top of the channel ($\langle\theta''\theta''\rangle^{1/2}/\Delta\Theta = 0.26$ at $z/H = 0.96$). Its minimum locates in the center core of the channel though the RMS vertical velocity fluctuation is maximum there.

Because of the adopted boundary conditions, both the mean vertical Reynolds stress $\langle u''w''\rangle$ and the mean vertical heat flux $\langle\theta''w''\rangle$ are zero at the wall and the top of the channel (Fig. 3b). The absolute magnitude of the mean vertical Reynolds stress increases with increasing wall-normal distance at the near-wall region whose maximum is $\langle u''w''\rangle/U^2 = 0.007$ at $z/H = 0.1$. It decreases linearly thereafter until the top of the channel. The mean vertical heat flux lies at its maximum ($\langle\theta''w''\rangle/(\Delta\Theta U) \approx 0.015$) for most of the channel height ($0.1 \leqslant z/H \leqslant 0.95$) that signifies the enhanced mixing and energy transport. It also explains the broad range of relatively constant temperature at the center core of the channel.

4.2. Mean plume heights

After reviewing the flow and turbulence structure in an unstably stratified open channel flow, the scalar plume transport behaviors will be discussed in this section. The mean plume heights $\bar{z}(x)$ and the vertical dispersion coefficients $\sigma_z(x)$ are discussed that also serve as model validation exercises.

The spatial distribution of the mean scalar mixing ratio $\langle c\rangle$ is used to derive the mean plume height in accordance with the following formula:

$$\bar{z}(x) = \frac{\int_0^H \langle c(x,z)\rangle z\,\mathrm{d}z}{\int_0^H \langle c(x,z)\rangle\,\mathrm{d}z}. \tag{6}$$

The plume meandering features in the form of ascending and descending scalar trajectories for different emission heights are contrasted in Fig. 4 by their mean plume heights. Also shown are the laboratory measurements by Willis and Deardorff [3–5], Briggs [41], and Weil et al. [7] together with the field measurements CONDORS appeared in van Haren and Nieuwstadt [42]. The streamwise distance shown in Fig. 4 is also made dimensionless by the convective mixed-layer scaling velocity as $X^* = (w^*/U)(x/H)$ [6].

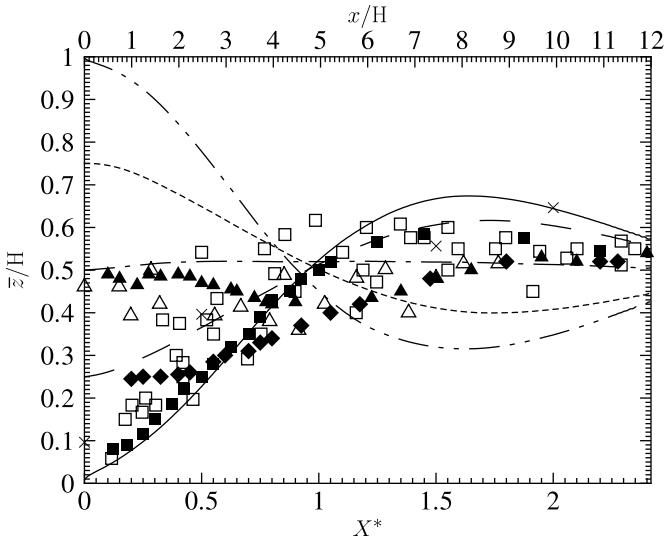

Fig. 4. Mean plume heights $\bar{z}/H$ expressed as functions of the streamwise distance x/H or X^* for emission heights z_s/H at 1: –···–, 0.75: ···, 0.5: –·–, 0.25: – – –, and 0: — calculated by the current DNS. z_s/H at 0 measured by Briggs [41]: □, z_s/H at 0.5 CONDORS data appeared in van Haren and Nieuwstadt [42]: △, z_s/H at 0.0 measured by Weil et al. [7]: ×, z_s/H at 0.5 measured by Willis and Deardorff [5]: ▲, z_s/H at 0.25 measured by Willis and Deardorff [4]: ◆, and z_s/H at 0.067 measured by Willis and Deardorff [3]: ■.

The scalar emitted at $z_s/H = 0.5$ does not have much agitation and travels close to the horizontal channel centerline in the streamwise direction. Its maximum mean plume rise ($\bar{z} - z_s$) is tiny ($0.02H$) occurring at $3 \leqslant x/H \leqslant 5$. Moreover, the maximum mean plume rise locates earlier than does the scalar emitted from other emission heights. The laboratory experiment performed by Willis and Deardorff [5] for an elevated source at the middle of the CBL shows an initial plume descent to $\bar{z}/z_i = 0.4$ at $X^* = 1$. Afterward, the plume is carried aloft back to the middle of the CBL. For the same emission height, though the CONDOR field measurements [42] are sparse, they exhibit plume meandering behaviors similar to those found by Willis and Deardorff [5]. The differences among the current DNS output, the laboratory measurements, and the field measurements should be attributed to the different temperature boundary conditions employed. The current DNS FEM model adopts a Dirichlet temperature boundary condition at the top of the channel so that a broad maximum of vertical heat flux is calculated at the center core of the channel. On the other hand, the physically modeled CBL [5] adopt stable stratification over the CBL in which the vertical heat flux decreases linearly with increasing height until the top of the CBL.

A remarkable plume ascent is observed for emission heights situated at the lower part of the channel. As calculated by the current DNS FEM model, the maximum mean plume height for emission heights at $z_s/H = 0.25$ is $\bar{z}/H = 0.6$ locating at $x/H = 8.5$, then it gradually descends toward the middle of the channel. The mean plume height measured by Willis and Deardorff [4] for the same emission

height also shows an initial plume ascent for $x/H \leqslant 9$ which is then followed by an overshoot at $x/H = 10$. The overshoot, whose maximum is $0.52z_i$, is about 20% smaller compared with that of the current DNS output. In addition, Willis and Deardorff [4] shows a farther distance for the plume ascent than does the current DNS FEM model.

In the current DNS calculation, the scalar from wall-level emission ($z_s/H = 0$) is carried aloft once being emitted into the channel. Its mean plume height passes through the middle altitude of the channel at $x/H = 5$ which is then followed by an overshoot of maximum mean plume height $\bar{z}/H = 0.68$ at $x/H = 8$. This maximum mean plume height is about 10% higher than that for the scalar emitted at $z_s/H = 0.25$. The DNS-calculated mean plume height is very close to that of the laboratory measurements [3] within its early development ($0 \leqslant X^* \leqslant 1$). However, the plume overshoot measured by Willis and Deardorff [3] is almost 15% lower than the present calculated value. It is worth mentioning that the wall-level emission height adopted by Willis and Deardorff [3] is not exactly at the bottom of the CBL but is elevated slightly at $z_s/z_i = 0.067$. The laboratory experiments performed by Briggs [41] and Weil et al. [7] also show initial plume ascents in CBLs. In particular, the maximum mean plume rise measured by Briggs [41] occurs earlier ($\bar{z}/z_i = 0.62$ at $X^* = 1$) than that determined by the current DNS output or Willis and Deardorff [3]. The mean plume height measured by Briggs [41], though its data points are sparse and scattering, passes through the middle of the CBL ($\bar{z}/z_i = 0.5$) at $X^* \approx 0.5$. Afterward, the plume continuously ascends and attains the maximum mean plume height $\bar{z}/z_i = 0.62$ at $X^* = 1$. The mean plume height eventually converges to the center of CBL thereafter because of thorough scalar mixing. The initial plume ascent of wall-level emission measured by Weil et al. [7] is close to that measured by Briggs [41]. It is thus higher as compared with that found by the current DNS FEM model or Willis and Deardorff [3].

Unlike the scalar emitted at the lower part of the channel, the current DNS output shows that the scalar emitted at a higher altitude ($z_s/H > 0.5$) descends rapidly after emission. The mean plume height for the scalar emitted at $z_s/H = 0.75$ passes through the channel center at $x/H = 5$ which is then followed by an overshoot downward to the minimum mean plume height $\bar{z}/H = 0.4$ at $x/H = 8.5$. The scalar emitted at $z_s/H = 1$ descends even faster to $\bar{z}/H = 0.32$ at $x/H = 8$. Eventually, the mean plume heights for both emissions converge gradually toward the center of the channel in the streamwise direction.

4.3. Vertical scalar dispersion coefficient

The vertical mean plume coverage can be measured by the vertical scalar dispersion coefficient $\sigma_z(x)$ defined as

$$\sigma_z^2(x) = \frac{\int_0^H \langle c(x,z)\rangle (z - \bar{z}(x))^2 \,\mathrm{d}z}{\int_0^H \langle c(x,z)\rangle \,\mathrm{d}z}. \tag{7}$$

The current DNS-calculated dispersion coefficients for different emission heights are expressed as functions of streamwise distance in Fig. 5. Also shown are the measurements collected by Willis and Deardorff [5], Briggs [41], and van Haren and Nieuwstadt [42]. For the emission heights tested, the dispersion coefficients exhibit similar behaviors that develop rapidly to values of $0.25 \leqslant \sigma_z/H \leqslant 0.3$ within $0 \leqslant x/H \leqslant 4$ followed by slight overshoots. These rapidly increasing dispersion coefficients in the vicinity of the sources represent the fast plume development in the near field. The maximum dispersion coefficients ($0.25 \leqslant \sigma_z/H \leqslant 0.3$) locate around the maximum plume meandering ($3 \leqslant x/H \leqslant 6$). Afterward, the dispersion coefficients converge gradually to $0.27 \leqslant \sigma_z/H \leqslant 0.29$ until the downstream outlet. For the scalars emitted at the center core of the channel ($z_s/H = 0.25$, 0.5, and 0.75), their dispersion coefficients are close to each other throughout the streamwise extent. These similar values are mainly due to the broad range of relatively constant vertical velocity fluctuation $w''w''$ throughout the center core of the channel. The current DNS-calculated dispersion coefficients are close to the laboratory results [5] and the field measurements [42] for $z_s/z_i = 0.5$. In particular, they fall within and agree reasonably well with the scattered data points collected in CBL experiments.

For the scalar emitted at $z_s/H = 0$, the dispersion coefficient in the near field ($x/H \leqslant 4$) is smaller than that of the higher emission heights discussed above. The reduced dispersion coefficient is mainly due to the smaller vertical velocity fluctuation at the near-wall region of the channel. The current DNS-calculated dispersion coefficient also lies within the sparse data points measured by Briggs [41]

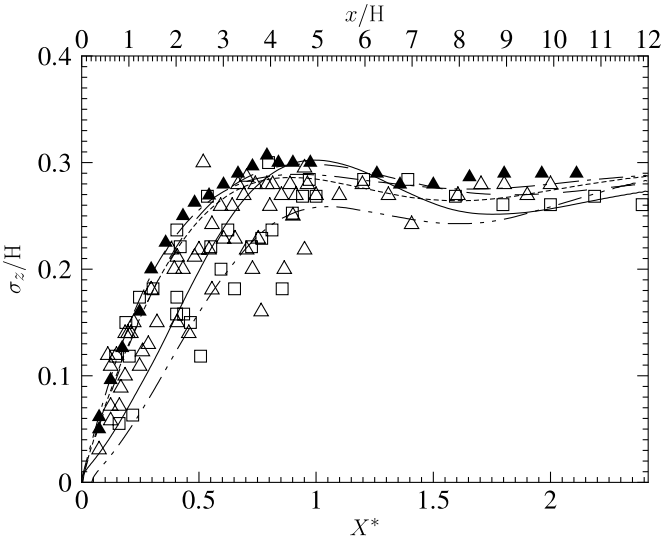

Fig. 5. Vertical dispersion coefficients σ_z/H expressed as functions of the streamwise distance x/H or X^* for emission heights z_s/H at 1: –···–, 0.75: ···, 0.5: –·–, 0.25: ––––, and 0: — calculated by the current DNS. z_s/H at 0 measured by Briggs [41]: □, z_s/H at 0.5 CONDORS data appeared in van Haren and Nieuwstadt [42]: △, and z_s/H at 0.5 measured by Willis and Deardorff [5]: ▲.

throughout the streamwise extent. In the early plume development regions, the DNS-calculated dispersion coefficient for the scalar emitted at $z_s/H = 1$ is smaller than that for the scalar emitted at $z_s/H = 0$. It is mainly due to the higher mean flow at the top of the channel, that enhances the scalar transport in the streamwise direction by advection but suppresses the crosswind vertical turbulent scalar transport. Eventually, behind the plume meandering range, the dispersion coefficients for the scalar emitted at $z_s/H = 0$ and 1 are similar to those emitted at the center core of the channel.

4.4. Spatial distribution of scalar mixing ratio

Fig. 6 depicts the spatial distributions of the mean scalar mixing ratio $\langle c \rangle$ on the x–z plane. The buoyancy effect due to vertical temperature gradient across the channel height leads to different scalar plume transport and meandering characteristics for different emission heights. This plume meandering poses tremendous impact on the assumption adopted in the conventional Gaussian plume models which assume no vertical plume meandering. The current DNS output shows plume descents for emission heights at $z_s/H = 1$ (Fig. 6a) and 0.75 (Fig. 6b). The plume reaches the channel bottom at $3 \leqslant x/H \leqslant 5$ that eventually develops local maximum scalar mixing ratio traveling near the wall until the downstream outlet. On the contrary, no noticeable plume meandering is determined for the scalar emitted at $z_s/H = 0.5$ (Fig. 6c). The scalar travels horizontally in the streamwise direction whose scalar mixing ratio is fairly even across the vertical extent of the channel for $x/H \geqslant 3$. In fact, the scalar emitted at the channel center exhibits the best mixing among the emission heights tested that is mainly due to the large vertical velocity fluctuation around its emission height. In contrast, remarkable plume rises are observed for the scalar emitted at the lower part of the channel at $z_s/H = 0.25$ (Fig. 6d) and 0 (Fig. 6e). The plume travels close to the wall until $4 \leqslant x/H \leqslant 5$ that leads to high wall-level scalar mixing ratio in the near field. It then ascends to the upper part of the channel that shifts the local maximum scalar mixing ratio from the lower to the upper parts of the channel. Finally, the plume travels horizontally in the streamwise direction at the upper part of the channel until leaving the downstream outlet.

4.5. Spatial distribution of root-mean-square scalar mixing ratio fluctuation

One of the merits of DNS is the accumulation of statistics from the database. The spatial distributions of the calculated RMS scalar mixing ratio fluctuation $\langle c''c'' \rangle^{1/2}$ for different emission heights are contrasted in Fig. 7. Generally, the RMS scalar mixing ratio fluctuation is high near the sources (because of the high scalar mixing ratio there) and decreases with increasing distance from the sources. Unlike the spatial distribution of the mean scalar mixing ratio, neither significant ascent nor significant descent of RMS scalar mixing ratio fluctuation is observed except

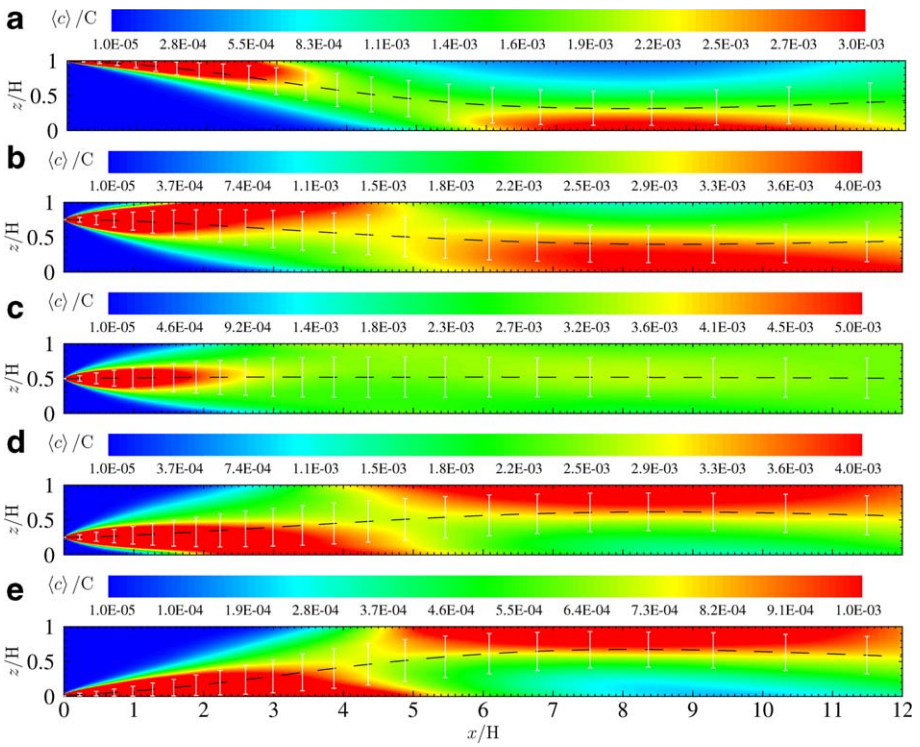

Fig. 6. Spatial contours of the mean scalar mixing ratio $\langle c \rangle / C$ for emission height z_s/H at (a) 1, (b) 0.75, (c) 0.5, (d) 0.25, and (e) 0. Also shown are the mean plume height $\bar{z}/H$: ––– and the mean plume width defined in terms of the mean vertical dispersion coefficient σ_z/H: white bars. The length of the bars is equal to $2\sigma_z/H$.

for the scalar emitted at $z_s/H = 1$. For this case, the trajectory of RMS scalar mixing ratio fluctuation follows the mean plume height that descends to the lower part of the channel (Fig. 7a). Along the mean plume height, high RMS scalar mixing ratio fluctuation ($\langle c''c''\rangle^{1/2} \geqslant 10^{-5}$) is observed for $x/H \leqslant 5$. The RMS scalar mixing ratio fluctuation is less than 10^{-6} C thereafter until leaving the downstream outlet. For the scalar emitted at the center core of the channel ($z_s/H = 0.25$, 0.5, and 0.75), the spatial distributions of the RMS scalar mixing ratio fluctuation exhibit comparable structures and values (Fig. 7b–d). For the scalar emitted at $z_s/H = 0$, the high RMS scalar mixing ratio fluctuation is close to the wall for $x/H < 2$ then extends toward the center core of the channel for $x/H \leqslant 4$ (Fig. 7e).

4.6. Spatial distribution of mean scalar fluxes

Turbulent scalar transport is represented mathematically by scalar flux $c''u_i''$. Analysis of scalar fluxes helps to enrich our understanding on the turbulent scalar transport behavior and the underneath mixing mechanism. Due to the periodic boundary condition adopted in the spanwise direction, the net turbulent scalar transport occurs only in the streamwise and vertical directions (vertical plane). In fact, because of the mean flow, the diffusive transport is negligible and the turbulent transport is tiny, compared with the scalar transport by advection in the streamwise direction.

4.6.1. Streamwise scalar flux

The spatial distributions of the mean streamwise scalar flux $\langle c''u''\rangle$ for different emission heights are illustrated in Fig. 8. The magnitude of the mean streamwise scalar flux is high near the source because of the large scalar mixing ratio there. For the scalar emitted at $z_s/H = 1$, the positive mean streamwise scalar flux descends from the source height to the lower part of the channel (Fig. 8a). As such, a local maximum of mean streamwise scalar flux ($\langle c''u''\rangle/(CU) \geqslant 10^{-5}$) is developed at $4 \leqslant x/H \leqslant 10$. On the other hand, the negative mean streamwise scalar flux also descends right after emission but no noticeable local minimum is developed until the downstream outlet. The mean streamwise scalar flux for the scalar emitted at the center core of the channel ($z_s/H = 0.75$, 0.5, and 0.25) exhibits similar spatial characteristics (Fig. 8b–d). It is positive and negative, respectively, below and above the emission height in the near field ($x/H \leqslant 3$). However, it shows different spatial characteristics in the far field. For the scalar emitted at $z_s/H = 0.75$, local positive maxima are developed at the top and bottom of the channel at $3 \leqslant x/H \leqslant 7$ (Fig. 8b) that signifies increasing streamwise velocity ($u'' > 0$) leading to increasing scalar mixing ratio ($c'' > 0$), and vice versa. For the scalar emitted at $z_s/H = 0.5$, the negative mean streamwise scalar flux ascends to the top of the channel at $1.5 \leqslant x/H \leqslant 4$ while the positive mean streamwise scalar flux descends from the emission height to the lower part of the channel and develops a

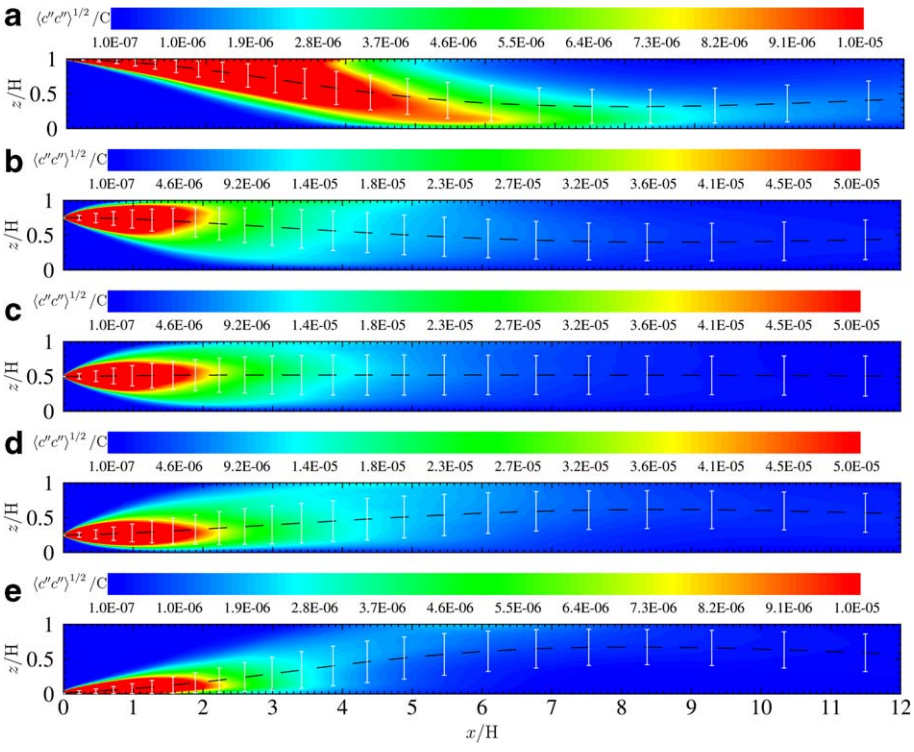

Fig. 7. Spatial contours of the root-mean-square scalar mixing ratio fluctuation $\langle c''c''\rangle^{1/2}/C$ for emission heights z_s/H at (a) 1, (b) 0.75, (c) 0.5, (d) 0.25, and (e) 0. Also shown are the mean plume height $\bar{z}/H$: – – – and the mean plume width defined in terms of the mean vertical dispersion coefficient σ_z/H: white bars. The length of the bars is equal to $2\sigma_z/H$.

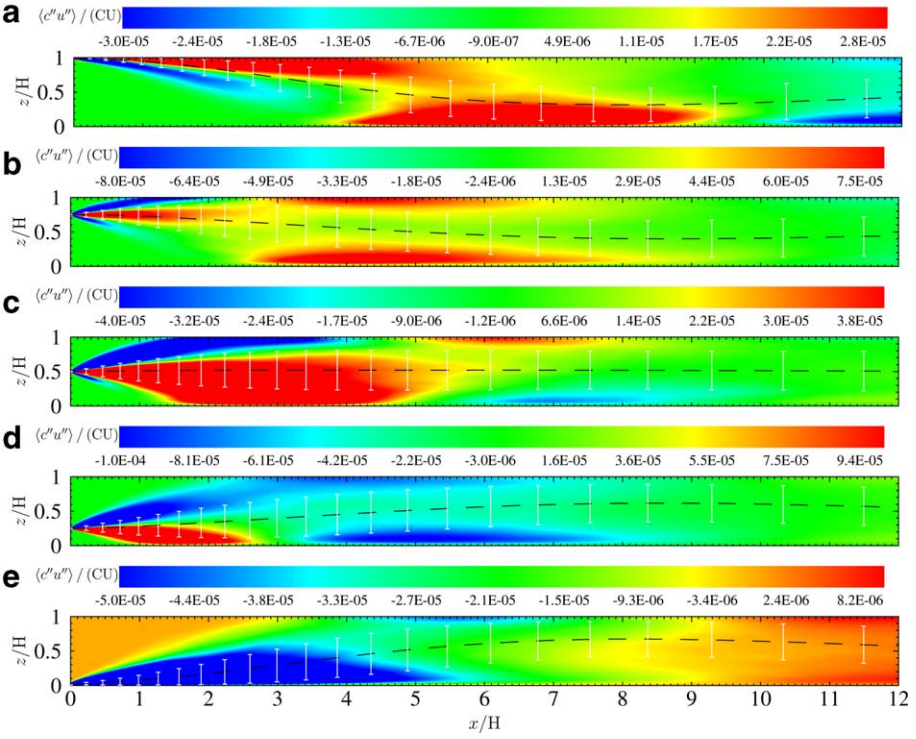

Fig. 8. Spatial contours of the mean streamwise scalar flux $\langle c''u''\rangle/(CU)$ for emission heights z_s/H at (a) 1, (b) 0.75, (c) 0.5, (d) 0.25, and (e) 0. Also shown are the mean plume height $\bar{z}/H$: ––– and the mean plume width defined in terms of the mean vertical dispersion coefficient σ_z/H: white bars. The length of the bars is equal to $2\sigma_z/H$.

broad area of local maximum ($\langle c''u''\rangle/(CU) \geqslant 2.0\times10^{-5}$) at $2 \leqslant x/H \leqslant 4$ covering almost 75% of the channel height (Fig. 8c). This positive mean streamwise scalar flux then ascends and develops a smaller area of local maximum at the top of the channel at $5.5 \leqslant x/H \leqslant 7.5$. Meanwhile, a small area of local minimum of negative mean streamwise scalar flux develops at the bottom of the channel at $6 \leqslant x/H \leqslant 8$. Though obvious spatial variation of mean streamwise scalar flux is observed, no noticeable plume meandering is observed from the spatial distribution of mean scalar mixing ratio for the emission height at $z_s/H = 0.5$ (Fig. 6c). For the scalar emitted at $z_s/H = 0.25$, the positive mean streamwise scalar flux descends and reaches the wall at $1 \leqslant x/H \leqslant 2.6$ while the negative mean streamwise scalar flux ascends and develops an extended local minimum ($2.3 \leqslant x/H \leqslant 7$) at the top of the channel (Fig. 8d). In addition, a wall-level local minimum of negative streamwise mean scalar flux is developed at further downstream ($3.5 \leqslant x/H \leqslant 8$). For the scalar emitted at $z_s/H = 0$, a broad area of minimum negative mean streamwise scalar flux is developed behind the source at the lower part of the channel at $x/H \leqslant 5.5$ (Fig. 8e). The negative mean streamwise scalar flux gradually changes to positive passing through the downstream outlet.

4.6.2. Vertical scalar flux

As shown in Fig. 9, the mean vertical scalar flux $\langle c''w''\rangle$ is generally positive and negative, respectively, above and below the mean plume heights for the emission heights tested. Hence, upward flow ($w'' > 0$) increases the scalar mixing ratio ($c'' > 0$), and vice versa, for regions over the mean plume height whilst upward flow ($w'' > 0$) decreases the scalar mixing ratio ($c'' < 0$) and vice versa, for regions below the mean plume heights. This characteristic structure of vertical scalar flux signifies the cross-stream turbulent scalar transport as well as the plume development and widening.

For the scalar emitted at $z_s/H = 1$, the negative mean vertical scalar flux descends from the emission height to the lower part of the channel as far as $x/H = 5$ (Fig. 9a). This descending negative mean vertical scalar flux brings scalar downward by turbulent transport. In fact, this structure of negative vertical scalar flux signifies the downward scalar transport even above the mean plume height that explains the rapid plume descent for the scalar emitted at $z_s/H = 1$. The scalar emitted at $z_s/H = 0$, however, shows the opposite phenomena. It exhibits a rapidly ascending positive mean vertical scalar flux right after emission until $x/H = 5$ (Fig. 9e). This ascent brings scalar upward from the wall to the upper part of the channel by vertical turbulent scalar transport that eventually raises the mean plume height from the lower to the upper parts of the channel. Moreover, only positive mean vertical scalar flux is calculated throughout the channel. As a result, the turbulent scalar transport is solely upward regardless of the regions that further supports the rapid plume rise.

The spatial distributions of the mean vertical scalar flux for the scalar emitted at the center core of the channel

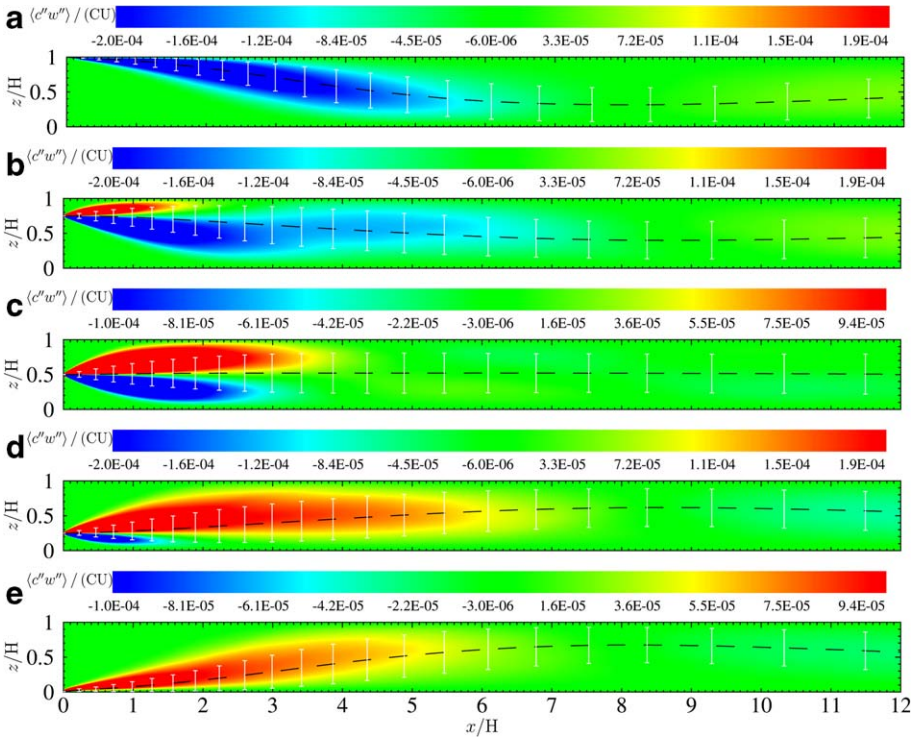

Fig. 9. Spatial contours of the mean vertical scalar flux $\langle c''w''\rangle/(CU)$ for emission heights z_s/H at (a) 1, (b) 0.75, (c) 0.5, (d) 0.25, and (e) 0. Also shown are the mean plume height $\bar{z}/H$: ––– and the mean plume width defined in terms of the mean vertical dispersion coefficient σ_z/H: white bars. The length of the bars is equal to $2\sigma_z/H$.

($z_s/H = 0.75$, 0.5, and 0.25) exhibit similar behaviors (Fig. 9b–d). Unlike that emitted at the top and the bottom of the channel, the scalar emitted at the center core shows both positive and negative mean vertical scalar fluxes so that the cross-stream turbulent scalar transport is not in a single direction. Their mean vertical scalar fluxes are positive and negative, respectively, above and below the mean plume heights. Hence, the scalar is brought away by turbulent scalar transport from the mean plume heights in the cross-stream direction. This cross-stream turbulent scalar transport also explains the widening of mean plume coverage and the plume development (as illustrated as $2\sigma_z/H$ in Fig. 6). The differences of the sizes and magnitudes between the positive and negative mean vertical scalar fluxes then contribute to the plume meandering. For the scalar emitted at $z_s/H = 0.5$, the size and magnitude of the positive vertical scalar flux is only slightly greater than its negative counterpart (Fig. 9c). Moreover, the mean vertical scalar flux along the mean plume height is negligible. Thus, the plume meandering is not noticeable as indicated in Fig. 6c. For the scalar emitted at $z_s/H = 0.25$, the positive mean vertical scalar flux ascends and develops a broad area of maximum almost covering the whole vertical extent of the channel until $x/H = 6$, whose size is much greater than that of the descending negative mean vertical scalar flux below the mean plume height (Fig. 9d). As a result, the plume is carried aloft (Fig. 6d). On the other hand, for the scalar emitted at $z_s/H = 0.75$, the negative mean vertical scalar flux descends right after emission until $x/H = 2$ then rebounds slightly at the center core of the channel (Fig. 9b). Eventually, it develops a broad area of negative minimum at $2 \leqslant x/H \leqslant 6$ covering the mean plume height whose size is greater than the maximum developed by its positive counterpart above the mean plume height ($x/H < 2$). The differences in sizes and magnitudes between the positive and negative mean vertical scalar fluxes signify the domination of downward turbulent scalar transport and thus explains the plume descent phenomenon (as illustrated in Fig. 6b). Conclusively, the negative (positive) mean vertical scalar flux covering the mean plume height at $1 \leqslant x/H \leqslant 6$ for an emission height at $x_s/H = 0.75$ (0.25) shows that the turbulent scalar transport is not away from the mean plume height but is solely downward (upward). These characteristic uni-directional mean vertical scalar fluxes explain the rapid plume descent (ascent) observed in unstably stratified TBLs.

4.7. Spatial distribution of correlation coefficients

The plume transport behaviors in CBLs can also be studied through the analysis of the correlation coefficient between the calculated variables ϕ and ψ which is defined as

$$R_{\phi\psi} = \frac{\langle \phi''\psi''\rangle}{\langle \phi''\phi''\rangle^{1/2}\langle \psi''\psi''\rangle^{1/2}}. \quad (8)$$

This section discusses the spatial distribution of the correlation coefficients among the streamwise and vertical

velocities, temperature, and scalar mixing ratio calculated by the current DNS FEM model.

4.7.1. Correlation coefficient between streamwise velocity and scalar mixing ratio R_{cu}

The spatial distributions of R_{cu} for different emission heights exhibit a wide range of values (Fig. 10). Generally, the scalar emitted at $z_s/H = 0.5$ has the smallest R_{cu} ($-0.3 \leqslant R_{cu} \leqslant 0.3$) indicating that the streamwise velocity and the scalar mixing ratio are least correlated. On the contrary, the scalar emitted at $z_s/H = 0$ has the largest R_{cu} ($-1.0 \leqslant R_{cu} \leqslant 1.0$) and thus the streamwise fluid flow and the scalar transport are closely coupled. For the scalar emitted at the upper part of the channel at $z_s/H = 1.0$ (Fig. 10a) and 0.75 (Fig. 10b), a broad range of positive R_{cu} covering the vertical extent of the channel is observed at $3 \leqslant x/H \leqslant 9$ in which local positive maxima are developed at the top and bottom of the channel. Lowering the emission height to $z_s/H = 0.5$ shifts the wall-level positive local maximum R_{cu} slightly upstream ($2 \leqslant x/H \leqslant 4$, Fig. 10c). Meanwhile, another positive local maximum R_{cu} occurring at the upper part of the channel at $6 \leqslant x/H \leqslant 8$ reduces in size and value to $R_{cu} = 0.2$. On the other hand, the negative R_{cu} ascending from the emission height to the top of the channel becomes more noticeable. In addition, another wall-level negative local minimum R_{cu} is initialized at $6 \leqslant x/H \leqslant 8$. The positive local maximum R_{cu} at the top of the channel no longer exists when the emission height is further lowered to $z_s/H = 0.25$ (Fig. 10d). The range of the wall-level negative local minimum R_{cu} is enlarged and shifts slightly upstream ($4 \leqslant x/H \leqslant 9$). In the near field ($1 \leqslant x/H \leqslant 3$), the descending positive R_{cu} shifts upstream while the ascending negative R_{cu} is enlarged and develops a broad area of local minimum at $3 \leqslant x/H \leqslant 8$ at the top of the channel. For the scalar emitted at $z_s/H = 0$, no positive R_{cu} is observed while a prolonged wall-level negative R_{cu} is developed at $0 \leqslant x/H \leqslant 7$ (Fig. 10e).

4.7.2. Correlation coefficient between vertical velocity and scalar mixing ratio R_{cw}

Fig. 11 depicts the spatial distribution of R_{cw} for the scalar emitted at different heights. As there is no vertical mean flow in the channel ($\langle w \rangle = 0$), most of the scalar is transported vertically by turbulence while negligible amount is by molecular diffusion. The vertical turbulent scalar transport, which is represented mathematically by the vertical scalar flux $c''w''$, dominates the mechanism of cross-stream scalar transport. Thus, the R_{cw} structure signifies the nature of vertical turbulent scalar transport and helps explaining the scalar plume meandering commonly observed in CBLs. Analogous to the nature of positive and negative mean vertical scalar fluxes $\langle c''w'' \rangle$, positive R_{cw} above and negative R_{cw} below the mean plume height signify, respectively, the upward and downward turbulent scalar transport. The spatial distribution of R_{cw} for the scalar emitted at

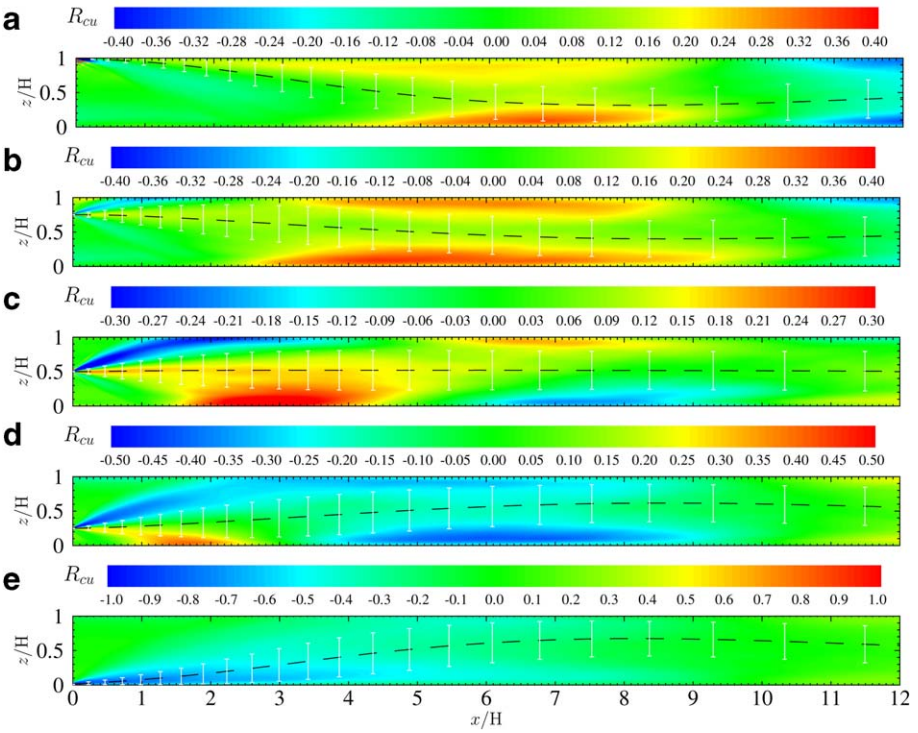

Fig. 10. Spatial contours of the correlation coefficient between streamwise velocity and scalar mixing ratio $R_{cu} = \langle c''u'' \rangle / \langle c''c'' \rangle^{1/2} / \langle u''u'' \rangle^{1/2}$ for emission heights z_s/H at (a) 1, (b) 0.75, (c) 0.5, (d) 0.25, and (e) 0. Also shown are the mean plume height $\bar{z}/H$: ––– and the mean plume width defined in terms of the mean vertical dispersion coefficient σ_z/H: white bars. The length of the bars is equal to $2\sigma_z/H$.

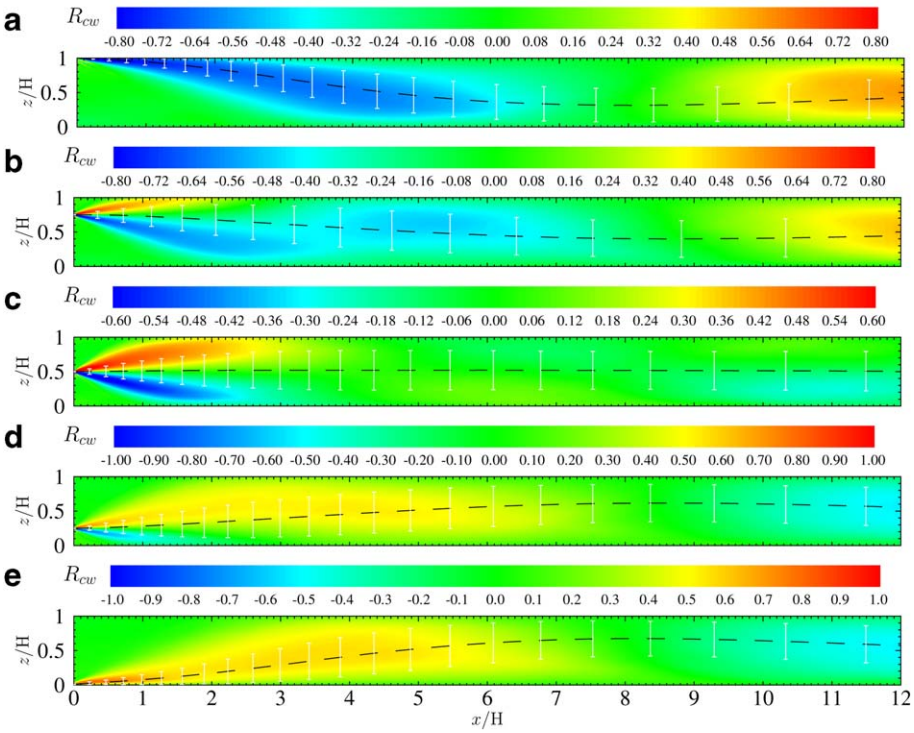

Fig. 11. Spatial contours of the correlation coefficient between vertical velocity and scalar mixing ratio $R_{cw} = \langle c''w''\rangle/\langle c''c''\rangle^{1/2}/\langle w''w''\rangle^{1/2}$ for emission heights z_s/H at (a) 1, (b) 0.75, (c) 0.5, (d) 0.25, and (e) 0. Also shown are the mean plume height $\bar{z}/H$: ––– and the mean plume width defined in terms of the mean vertical dispersion coefficient σ_z/H: white bars. The length of the bars is equal to $2\sigma_z/H$.

$z_s/H = 1$ shows that the fluid and scalar motions are closely coupled for $x/H \leqslant 6$ ($-0.7 \leqslant R_{cw} \leqslant -0.6$, Fig. 11a). The calculated broad area of negative R_{cw} helps explaining the remarkable plume descent phenomenon as depicted in Fig. 6a. Lowering the emission height to $z_s/H = 0.75$ then the R_{cw} above the mean plume height is positive for $x/H \leqslant 2$ (Fig. 11b). Meanwhile, the negative R_{cw} descends to the lower channel after emission until $x/H = 3$ which is then followed by a slight overshoot at the center core of the channel at $x/H = 5$. The negative local minimum R_{cw} at $3 \leqslant x/H \leqslant 8$, which covers the mean plume height and even most of the vertical extent of the channel, helps explaining the plume descent for the scalar emitted at $z_s/H = 0.75$. The scalar emitted at $z_s/H = 0.5$ shows a quite symmetric spatial distribution of R_{cw} above and below the mean plume height (Fig. 11c). Neither domination of positive nor negative R_{cw} is found. This finding supports the cross-stream turbulent scalar transport and the enlarging plume coverage with minor plume meandering. The scalar emitted at $z_s/H = 0.25$ exhibits a broad positive maximum R_{cw} at the center core of the channel for $x/H \leqslant 6$ (Fig. 11d), whose coverage over the mean plume height signifies the solely upward mean scalar turbulent transport and thus explains the plume rise from the lower to the upper parts of the channel. No negative R_{cw} is calculated for the scalar emitted at $z_s/H = 0$ (Fig. 11e). Instead, a broad area of positive maximum ($R_{cw} \geqslant 0.6$), covering almost the whole vertical extent of the channel for $x/H \leqslant 6$, is calculated. Hence, the (vertical) fluid and scalar motions are closely coupled. Based on these characteristics, the mean turbulent scalar transport is solely upward that explains the remarkable plume ascent for the scalar emitted at $z_s/H = 0$.

Conclusively, as determined by the current DNS FEM model, the negative (positive) R_{cw} for emission heights at the upper (lower) part of the channel covers the regions both above and below the mean plume height. This finding signifies that the vertical turbulent scalar transport is in a single direction regardless of its position and thus contributes to the plume meandering in unstably stratified TBLs.

4.7.3. Correlation coefficient between temperature and scalar mixing ratio $R_{c\theta}$

As the vertical plume meandering in unstably stratified TBLs is caused by the vertical temperature gradient and the buoyancy-generated turbulence of the ambient air, looking into the structure of $R_{c\theta}$ helps gaining more insight into the mechanism of plume meandering. As positive (negative) temperature fluctuation $\theta'' > 0$ ($\theta'' < 0$) leads to upward $\omega'' > 0$ (downward $\omega'' < 0$) fluid motions and so does turbulent scalar transport, the spatial distribution of $R_{c\theta}$ (Fig. 12) is similar to its R_{cw} counterpart (Fig. 11). In fact, the values of $R_{c\theta}$ ($-1 \leqslant R_{c\theta} \leqslant 1$) are comparable to those of R_{cw} so that the scalar motions follow closely the temperature fluctuation, and supports that the plume meandering is driven by buoyancy.

As shown in Fig. 12a for the scalar emitted at $z_s/H = 1$, the negative local minimum $R_{c\theta}$ follows the descending

mean plume height in which the magnitude of the (negative) $R_{c\theta}$ is high ($-1.0 \leqslant R_{c\theta} \leqslant -0.6$). Showing in Fig. 12b is the spatial distribution of $R_{c\theta}$ for the scalar emitted at $z_s/H = 0.75$. In the near field ($x/H \leqslant 3$), an ascending positive and a descending negative $R_{c\theta}$ are shown, respectively, above and below the mean plume height. Moreover, following the rebound of the descending negative $R_{c\theta}$, a broad area of negative local minimum ($-0.6 \leqslant R_{c\theta} \leqslant -0.5$) is developed at $5 \leqslant x/H \leqslant 8$ covering nearly the full vertical extent of the channel. This broad area of negative minimum $R_{c\theta}$ shows that an increase in temperature ($\theta'' > 0$) leads to a decrease in scalar mixing ratio ($c'' < 0$), and vice versa, for the scalar emitted at the upper part of the channel. The scalar emitted at the channel center ($z_s/H = 0.5$) shows an ascending positive $R_{c\theta}$ above the mean plume height and a descending negative $R_{c\theta}$ below (Fig. 12c). The positive and negative $R_{c\theta}$ are of comparable sizes and magnitudes that signify the cross-stream scalar transport in the near field ($x/H \leqslant 4$). In the far field ($6 \leqslant x/H \leqslant 9$), local extremities of positive and negative $R_{c\theta}$ reside at the bottom and the top of the channel, respectively. The value of $R_{c\theta}$ is small (almost zero) along the mean plume height (at the center core of the channel), thus, the scalar motions are not affected much by the buoyancy and no noticeable plume meandering is observed (Fig. 6c). The scalar emitted at $z_s/H = 0.25$ (Fig. 12d) and 0 (Fig. 12e) shows a broad range of positive $R_{c\theta}$ almost fully covering the vertical extent of the channel. In particular, the value of $R_{c\theta}$ is positive and high ($0.7 \leqslant R_{c\theta} \leqslant 0.8$) so the scalar motions closely follow the temperature fluctuation in the ascending plume. These findings are opposite to the $R_{c\theta}$ structures for the scalar emitted at the upper part of the channel that increase in temperature ($\theta'' > 0$) leads to increase in scalar mixing ratio ($c'' > 0$), and vice versa. It is worth mentioning that the local maximum (minimum) positive (negative) $R_{c\theta}$ for the scalar emitted at $z_s/H = 0.75$ and 0.25 is closer to the wall than that of R_{wc}.

4.8. Scalar mixing ratio budget

Taking the ensemble average of conservation of mass expressed by Eq. (4) yields the budget equation of scalar mixing ratio transport

$$\frac{\partial\langle c\rangle}{\partial t} = \underbrace{-\langle u\rangle\frac{\partial\langle c\rangle}{\partial x}}_{\text{streamwise advection}} \overbrace{\underbrace{-\frac{\partial}{\partial x}\langle u''c''\rangle}_{\text{streamwise}} \underbrace{-\frac{\partial}{\partial z}\langle w''c''\rangle}_{\text{vertical}}}^{\text{turbulent transport}} + \overbrace{\frac{1}{ReSc}\left(\underbrace{\frac{\partial^2\langle c\rangle}{\partial x^2}}_{\text{streamwise}} + \underbrace{\frac{\partial^2\langle c\rangle}{\partial z^2}}_{\text{vertical}}\right)}^{\text{molecular diffusion}}. \tag{9}$$

The assumption of periodic scalar boundary condition in the spanwise direction makes all the terms in the y-direction vanish. The term on the left-hand-side of Eq. (9) is the temporal derivation of the mean scalar mixing ratio whose ensemble average is equal to zero in quasi-steady state. The first and second terms on the right-hand-side

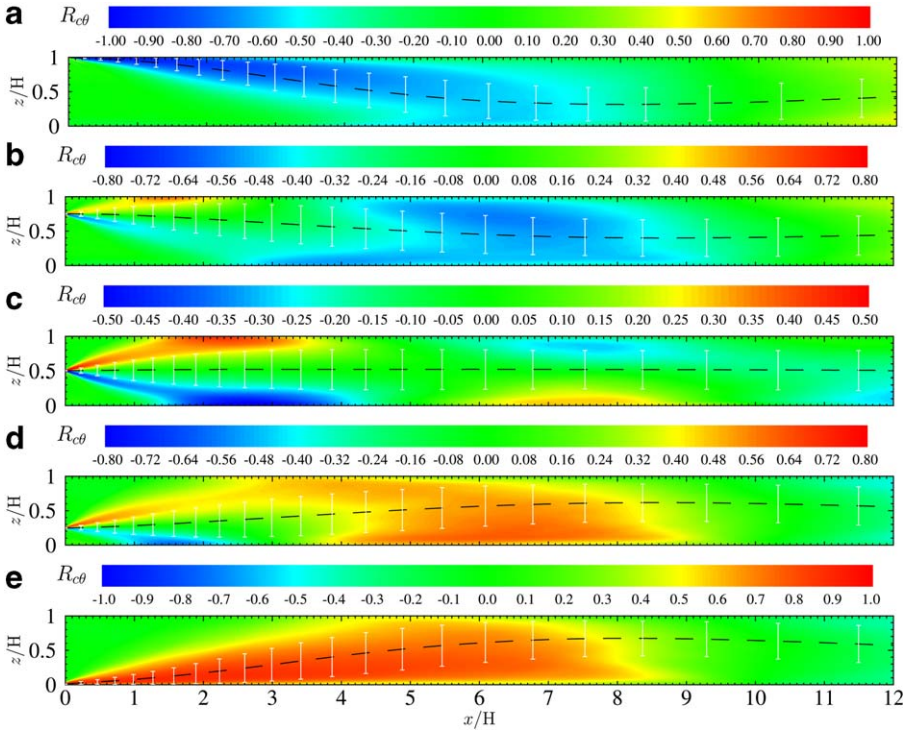

Fig. 12. Spatial contours of the correlation coefficient between temperature and scalar mixing ratio $R_{c\theta} = \langle c''\theta''\rangle/\langle c''c''\rangle^{1/2}/\langle\theta''\theta''\rangle^{1/2}$ for emission heights z_s/H at (a) 1, (b) 0.75, (c) 0.5, (d) 0.25, and (e) 0. Also shown are the mean plume height $\bar{z}/H$: ––– and the mean plume width defined in terms of the mean vertical dispersion coefficient σ_z/H: white bars. The length of the bars is equal to $2\sigma_z/H$.

are the scalar transport in the streamwise direction by mean flow and turbulence, respectively. The third term represents the turbulent scalar transport in the vertical (cross-stream) direction. The fourth and fifth term represent the diffusive scalar transport in the streamwise and vertical directions, respectively. The relative contributions of the terms in Eq. (9) help investigating the mechanism of the scalar transport and mixing in CBLs.

The spatial distributions of the terms defined in Eq. (9) are depicted in Figs. 13 and 14, respectively, for the scalar emitted at $z_s/H = 1$ and $z_s/H = 0$. Not shown in the figures are the contributions by molecular diffusion which are at least an order of magnitude smaller than those of the other terms. The unsmooth patterns shown in Fig. 13 and 14 are mainly due to the small scales of the derived variables especially at region of changing sign. Nevertheless, the results are able to illustrate the characteristic structure of the contribution from different terms in the mass conservation equation. Most of the scalar transport is due to streamwise advection $-\langle u\rangle\partial\langle c\rangle/\partial x$ and vertical turbulent scalar transport $-\partial\langle w''c''\rangle/\partial z$. The scalar transport in the streamwise direction by horizontal turbulent scalar transport $-\partial\langle u''c''\rangle/\partial x$ is small that is about 1/4 of that by streamwise advection. Hence, The streamwise advection and vertical turbulent scalar transport terms generally counter-balance each other. As a result, the scalar transport mechanism can be explained by the interaction between the advection in the streamwise direction and the turbulent transport in the vertical direction.

For the scalar emitted at $z_s/H = 1$, the mean plume height is around the trajectory of zero streamwise scalar advection or zero vertical turbulent diffusion (Fig. 13). The streamwise advection is positive and negative, respectively, above and below the mean plume height. The spatial

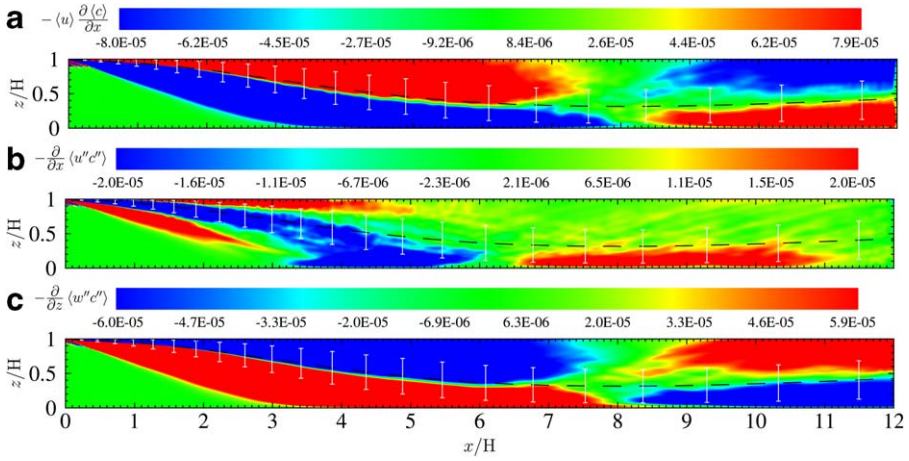

Fig. 13. Spatial contours of the terms in the mean scalar mixing ratio budget balance Eq. (9) for emission height z_s/H at 1. (a) streamwise advection $-\langle u\rangle\partial\langle c\rangle/\partial x$, (b) streamwise turbulent transport $-\partial\langle u''c''\rangle/\partial x$, and (c) vertical turbulent transport $-\partial\langle w''c''\rangle/\partial z$. Also shown are the mean plume height $\bar{z}/H$: ––– and the mean plume width defined in terms of the mean vertical dispersion coefficient σ_z/H: white bars. The length of the bars is equal to $2\sigma_z/H$.

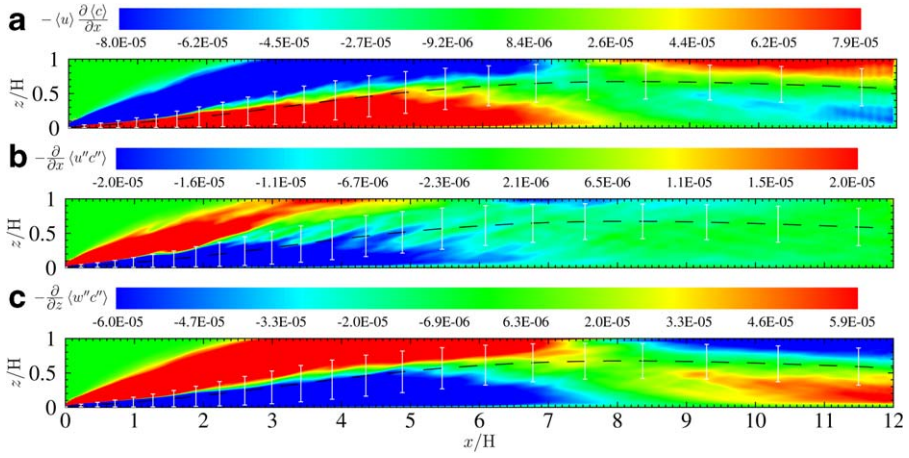

Fig. 14. Spatial contours of the terms in the mean scalar mixing ratio budget balance Eq. (9) for emission height z_s/H at 0. (a) streamwise advection $-\langle u\rangle\partial\langle c\rangle/\partial x$, (b) streamwise turbulent transport $-\partial\langle u''c''\rangle/\partial x$, and (c) vertical turbulent transport $-\partial\langle w''c''\rangle/\partial z$. Also shown are the mean plume height $\bar{z}/H$: ––– and the mean plume width defined in terms of the mean vertical dispersion coefficient σ_z/H: white bars. The length of the bars is equal to $2\sigma_z/H$.

distribution of the vertical turbulent scalar transport exhibits the opposite behaviors. This finding further supports the counter-balancing behaviors between the streamwise scalar advection and the vertical turbulent scalar transport in scalar plume. The region of positive streamwise advection is hereby defined as the core region of the plume where the scalar is transported from the upstream by streamwise advection. The scalar is then removed from the core region in the vertical (cross-stream) direction by vertical turbulent scalar transport. The scalar emitted at the wall (Fig. 14) and the center core of the channel (not shown here) also exhibits the similar plume transport characteristics. Hence, the basic scalar movement in plume scalar transport is established.

The mean plume height for the scalar emitted at $z_s/H = 0$ follows closely the trajectories of zero streamwise scalar advection and zero vertical turbulent scalar transport (Fig. 14). The characteristic of scalar mixing ratio budget generally follows the basic one discussed previously for emission height at $z_s/H = 1$. As shown in Fig. 14, the streamwise advection brings scalar from upstream to the wall-level core region. The broad negative vertical turbulent scalar transport below the mean plume height, which coincides with the core region of the plume, contributes to the upward turbulent scalar transport and the plume ascent. The locations of positive and negative vertical turbulent scalar transport reverse in the far field ($x/H \geqslant 8$) that signifies the thorough scalar mixing near the downstream outlet.

Not shown here are the spatial distributions of the terms of scalar mixing ratio budget for emission heights at the center core of the channel ($z_s/H = 0.75$, 0.5, and 0.25). Their behaviors generally follows those for emission heights discussed above ($z_s/H = 0.0$ and 1.0) and thus the discussion is not repeated again.

4.9. Instantaneous fields

The previous sections discuss the behaviors of mean quantities that explain the mechanism of characteristic scalar plume meandering in an unstably stratified open channel flow. Additional perspective of turbulent scalar transport and plume meandering mechanism can be obtained by looking into the snapshot of instantaneous fields. The snapshots calculated by the current DNS FEM model are considered as typical flow and scalar transport structures.

The perspective views of isosurfaces of fluctuating vertical velocity w'' are shown in Fig. 15. Also shown are the spatial distributions of the temperature θ on these isosurfaces. As shown by the current DNS output, the vertical fluid motions are generally driven by buoyancy such that

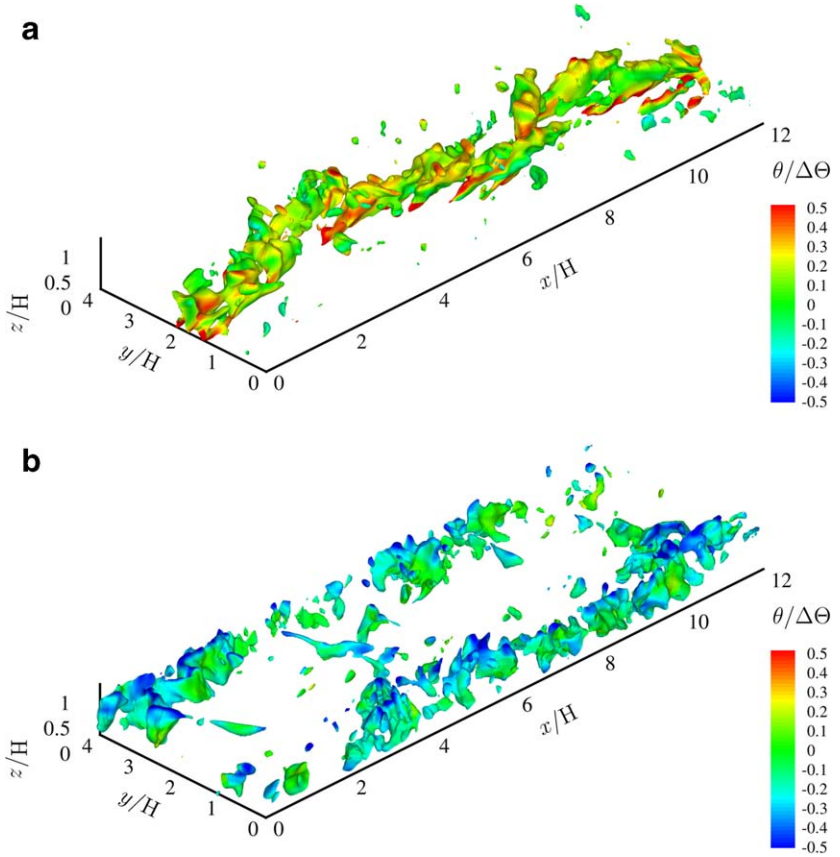

Fig. 15. Perspective views of the isosurfaces of constant instantaneous vertical fluctuating velocity w''/U. (a) $w''/U = 0.1$ and (b) $w''/U = -0.1$. Also shown are the spatial contours of instantaneous temperature $\theta/\Delta\Theta$ on the isosurfaces.

upward flow are due to higher temperature while downward flow are due to lower temperature. Similar to the finding by Schmidt and Schumann [1], the current DNS FEM model calculates large scale updraft of hot fluid ($\theta/\Delta\Theta > 0$) moving upward (Fig. 15a) which is surrounded by small scale downdraft of cold fluid ($\theta/\Delta\Theta < 0$) moving downward (Fig. 15b). The plume meandering in unstably stratified TBLs is generally due to buoyancy such that hot updraft and cold downdraft drive the scalar upward and downward, respectively.

More perspective of the plume meandering behavior and mechanism is depicted in the instantaneous plume transport behavior in unstably stratified TBLs. Figs. 16 and 17 depict the perspective views of isosurfaces of instantaneous scalar mixing ratio for emission heights at $z_s/H = 1$ and 0, respectively. Also shown are the spatial distributions of the temperature on these isosurfaces. Partly because of the angle of views, most of the scalar shown in the figures is cold. Actually, the scalar temperature is generally cold above the plume at the upper part of the channel and is

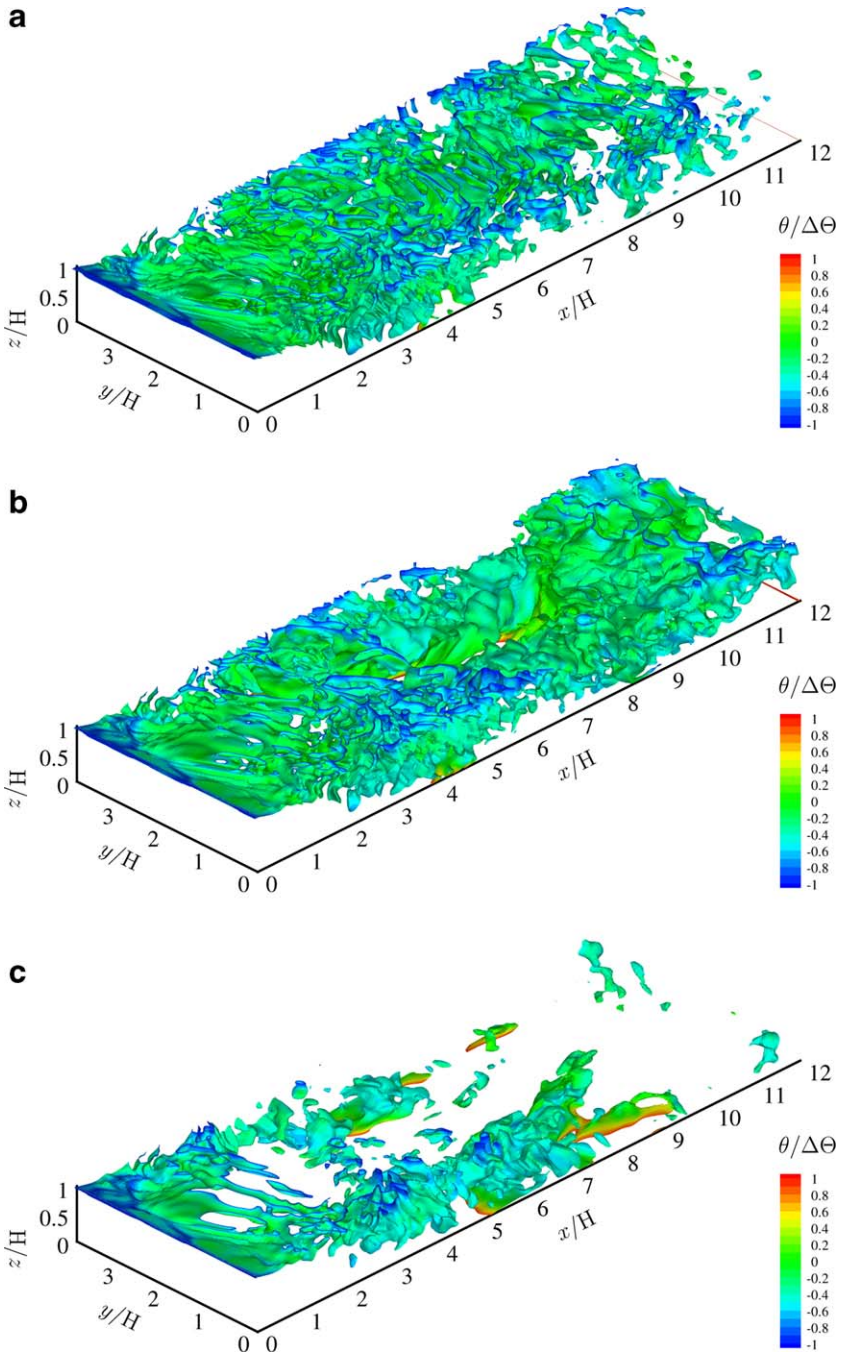

Fig. 16. Perspective views of the isosurfaces of constant instantaneous scalar mixing ratio c/C for emission height z_s/H at 1. (a) $c/C = 0.0001$, (b) $c/C = 0.001$, and (c) $c/C = 0.005$. Also shown are the spatial contours of instantaneous temperature $\theta/\Delta\Theta$ on the isosurfaces.

generally hot below the plume at the lower part of the channel. Not shown here are the instantaneous fields of scalar mixing ratio and temperature for emission heights at the center core of the channel. Nonetheless, the discussion in this section is also applicable to the scalar emitted at these emission heights.

For the scalar emitted at $z_s/H = 1$, the plume of smaller scalar mixing ratio, as illustrated by the isosurfaces, travels horizontally in the streamwise direction with a minor part of the plume descends to the lower part of the channel (Fig. 16a and b), while the plume of high scalar mixing ratio shows a more remarkable descent (Fig. 16c). This plume behavior leads to the overall plume descent as described previously. The scalar motions follow closely the fluctuating vertical velocity because the plume descends more rapidly near the side ($y/H \leqslant 1$ or $y/H \geqslant 3$) of the open channel (Fig. 16c).

In contrast, a rapid plume rise is illustrated in Fig. 17 for the scalar emitted at $z_s/H = 0$ in the form of isosurfaces of constant scalar mixing ratio. Analogous to the behavior of

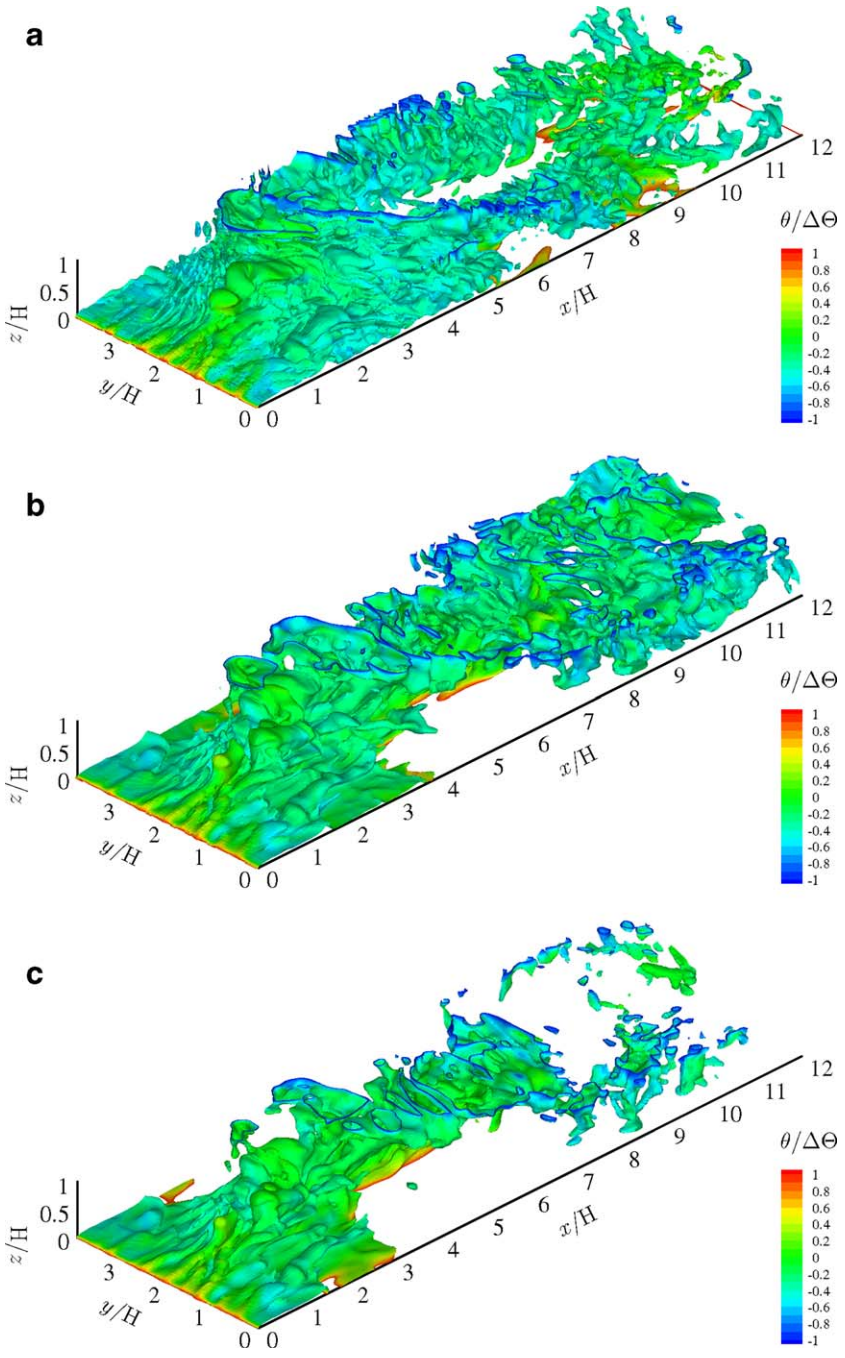

Fig. 17. Perspective views of the isosurfaces of constant instantaneous scalar mixing ratio c/C for emission height z_s/H at 0. (a) $c/C = 0.0001$, (b) $c/C = 0.001$, and (c) $c/C = 0.002$. Also shown are the spatial contours of instantaneous temperature $\theta/\Delta\Theta$ on the isosurfaces.

the scalar emitted at $z_s/H = 1$, the temperature above the plume is cold while below is hot. The vertical scalar transport generally follows the fluctuating vertical velocity so that the plume rises faster at the center of the channel ($1 \leqslant y/H \leqslant 3$). After the rapid plume rise, the plume of smaller scalar mixing ratio descends slightly back to the center core of the channel following the downward fluctuating vertical velocity at the side of the channel (Fig. 17a). On the other hand, the plume of higher scalar mixing ratio continue to travel to the upper part of the channel until the downstream outlet (Fig. 17b and c). The overall plume behavior then makes up the plume rise.

5. Conclusions

In this study, the turbulent transport of passive and inert scalar emitted from line sources at different heights in an unstably stratified open channel flow (heating at the bottom) is investigated. DNS is employed to model the fluid turbulence, temperature, and scalar mixing ratio by considering the incompressible Navier–Stokes and continuity, energy conservation, and mass conservation, respectively. Line sources are placed parallel to the spanwise direction at $z_s/H = 0$, 0.25, 0.5, 0.75, and 1 to investigate the scalar transport behaviors and the underneath plume meandering mechanisms.

The vertical profiles of mean streamwise velocity and mean temperature exhibit a broad range of relatively constant value at the center core of the channel which is mainly attributed to the enhanced mixing due to buoyancy-generated turbulence. Increased RMS velocity and temperature fluctuations, vertical Reynolds stress, and vertical heat flux also support the increased TKE in an unstably stratified TBLs.

Also serving as the model validation exercises, the current DNS-calculated mean plume heights and dispersion coefficients agree reasonably well with other laboratory and field measurements available in literature. Except the scalar emitted at the channel center ($z_s/H = 0.5$), which shows an unnoticeable plume meandering, a remarkable plume meandering in the form of plume ascent and descent is calculated for the emission heights tested. The plume ascends (descends) rapidly from the lower (upper) part of the channel that brings scalar upward (downward) to the upper (lower) part of the channel. The plume ascent (descent) is followed by an overshoot above (below) the channel center before converging to the channel center. The current DNS-calculated dispersion coefficients also agree reasonably well with laboratory and field measurements. The plume meandering is also depicted by the spatial distributions of the mean scalar mixing ratio together with its RMS fluctuation on the x–z plane for different emission heights that illustrates the switches of the plume trajectory between the upper and lower parts of the channel.

Because of the mean flow, most of the scalar transported in the streamwise direction is handled by advection rather than turbulent scalar transport. Whilst, because there is no mean flow in the vertical direction, the vertical turbulent scalar transport plays an essential role in the plume meandering behaviors in CBLs. For the scalar emitted at $z_s/H = 0.5$, the positive and negative vertical scalar fluxes, respectively, above and below the mean plume height signify that the cross-stream turbulent scalar transport brings scalar away from the mean plume height for plume development and widening. For the scalar emitted at the lower part of the channel at $z_s/H = 0.25$ and 0, sizes and magnitudes of the positive vertical scalar flux are larger than those of its negative counterpart. Hence, the vertical turbulent scalar transport is solely upward regardless of the position and it explains the plume rise in CBLs. A similar rationale applies to explain the plume descent for scalar emitted at the upper part of the channel.

By looking into the scalar mixing ratio budget balance, the contribution from molecular diffusion is found negligible. Whereas, the contribution from turbulent streamwise scalar transport is about 25% of that from streamwise advection. The contribution from streamwise advection and turbulent vertical scalar transport counter-balance each other. Based on the structure of the contribution from streamwise advection and turbulent vertical scalar transport, the region of positive streamwise advection is hereby defined as the core region of plume transport. We then establish the basic transport mechanism in scalar plume. The scalar in the core region is supplied from upstream by streamwise advection. It is then removed from the core region by cross-stream turbulent scalar transport that develops and widens the plume coverage.

Instantaneous snapshots are also employed to investigate the plume meandering mechanisms. A coherent structure consisting of updraft and downdraft are calculated by the current DNS FEM model. Snapshots of spatial distribution of scalar mixing ratio, similar to its mean properties, also show vertical plume meandering. In particular, the plume of higher scalar mixing ratio exhibits a more rapid ascent or descent as compared with that of the lower scalar mixing ratio.

Acknowledgements

The authors thank the Computer Centre of the University of Hong Kong for accessing their High Performance Computing Clusters. In particular, we are grateful to Mr. W.-K. Kwan and Mr. C.-M. Woo for their kind assistance during the development of the DNS FEM code.

References

[1] H. Schmidt, U. Schumann, Coherent structure of the convective boundary layer derived from large-eddy simulation, J. Fluid Mech. 200 (1989) 511–562.

[2] G.E. Willis, J.W. Deardorff, A laboratory model for the unstable boundary layer, J. Atmos. Sci. 31 (1974) 1297–1307.

[3] G.E. Willis, J.W. Deardorff, A laboratory model of diffusion into the convective planetary layer, Quart. J. Roy. Meteor. Soc. 102 (1976) 427–445.

[4] G.E. Willis, J.W. Deardorff, A laboratory study of dispersion from an elevated source within a modeled convective planetary boundary layer, Atmos. Environ. 12 (1978) 1305–1311.
[5] G.E. Willis, J.W. Deardorff, A laboratory study of dispersion from a source in the middle of the convectively mixed layer, Atmos. Environ. 15 (1981) 109–117.
[6] J.W. Deardorff, Laboratory experiment on diffusion: the use of convective mixed-layer scaling, J. Climate Appl. Meteor. 24 (1985) 1143–1151.
[7] J.C. Weil, W. Synder, R.E. Lawson Jr., M.S. Shipman, Experiments on buoyant plume dispersion in a laboratory convection tank, Bound.-Layer Meteor. 102 (2002) 367–414.
[8] E. Fedorovich, J. Thäter, A wind tunnel study of gaseous tracer dispersion in the convective boundary layer capped by a temperature inversion, Atmos. Environ. 36 (2002) 2245–2255.
[9] W.-Y. Sun, C.-Z. Chang, Diffusion model for a convective layer. Part II: Plume released from a continuous point source, J. Climate Appl. Meteor. 25 (1986) 1453–1463.
[10] P. Pai, T.H. Tsang, A finite element solution to turbulent diffusion in a convective boundary layer, Int. J. Numer. Methods Fluids 12 (1991) 179–195.
[11] C.-H. Liu, D.Y.C. Leung, Turbulence and dispersion studies using a three-dimensional second-order closure Eulerian model, J. Appl. Meteor. 40 (2001) 92–112.
[12] J.W. Deardorff, Numerical investigation of neutral and unstable planetary boundary layers, J. Atmos. Sci. 29 (1972) 91–115.
[13] C.-H. Moeng, A large-eddy-simulation model for the study of planetary boundary-layer turbulence, J. Atmos. Sci. 41 (1984) 2052–2062.
[14] R.I. Sykes, D.-S. Henn, Large-eddy simulation of turbulent sheared convection, J. Atmos. Sci. 46 (1989) 1106–1118.
[15] C.-H. Moeng, P.P. Sullivan, A comparison of shear- and buoyancy-driven planetary boundary layer flows, J. Atmos. Sci. 51 (1994) 999–1022.
[16] R.G. Lamb, Diffusion in the convective boundary layer, in: F.T.M. Nieuwstadt, H. van Dop (Eds.), Atmospheric Turbulence and Air Pollution Modelling, Reidel, 1982, pp. 159–229.
[17] J.C. Weil, Dispersion in a rapidly evolving convective boundary layer, in: Tenth Symposium on Turbulence and Diffusion, American Meteorological Society, 1992.
[18] J.C. Weil, P.P. Sullivan, C.-H. Moeng, Lagrangian modeling of dispersion in convective boundary layers with varying degrees of wind shear, in: Proceedings of the 2001 International Symposium on Environmental Hydraulics, ISEH and IAHR, 29 September to 2 October 2001.
[19] P.-J. Mason, Large-eddy simulation of dispersion in convective boundary layers with wind shear, Atmos. Environ. 26A (1992) 1561–1571.
[20] A. Dosio, J.V.-G. de Arellano, A.A.M. Holtslag, P.J.H. Builtjes, Dispersion of a passive tracer in buoyancy- and shear-driven boundary layers, J. Appl. Meteor. 42 (2003) 1116–1130.
[21] C. Fureby, G. Taber, H.G. Weller, A.D. Gosman, A comparative study of subgrid scale model in homogeneous isotropic turbulence, Phys. Fluids 9 (1997) 1416–1429.
[22] J.S. Smagorinsky, General circulation experiments with primitive equations, Mon. Weather Rev. 94 (1963) 99–152.
[23] U. Schumann, Subgrid scale model for finite difference simulation of turbulent flows in plane channels and annuli, J. Fluid Mech. 18 (1975) 376–404.
[24] M. Germano, U. Piomelli, P. Moin, W.H. Cabot, A dynamic subgrid-scale eddy viscosity model, Phys. Fluids A 3 (1991) 1760–1765.
[25] Y. Zang, R.L. Street, J.R. Koseff, A dynamic mixed subgrid-scale model and its application to turbulent recirculating flows, Phys. Fluids A 5 (1993) 3186–3196.
[26] S. Ghosal, T.S. Lund, P. Moin, K. Akselvoll, A dynamic localization model for large eddy simulation of turbulent flows, J. Fluid Mech. 286 (1995) 229–255.
[27] J. Kim, P. Moin, Transport of passive scalar in a turbulent channel flow, in: J.-C. Andre, J. Cousteix, F. Durst, B.E. Launder, F.W. Schmidt, J.H. Whitelaw (Eds.), Turbulent Shear Flow, vol. 6, Springer-Verlag, Berlin, 1989, pp. 85–96.
[28] J.-D. Li, R.W. Bilger, The diffusion of conserved and reactive scalars behind line sources in homogeneous turbulence, J. Fluid Mech. 318 (1996) 339–372.
[29] D. Livescu, F.A. Jaberi, C.K. Madnia, Passive-scalar wake behind a line source in grid turbulence, J. Fluid Mech. 416 (2000) 117–149.
[30] R. Barrett, M. Berry, T. Chan, J. Demmel, J. Donato, J. Dongarra, V. Eijkhout, R. Pozo, C. Romine, H. Van der Vorst, Templates for The Solution of Linear Systems: Building Blocks for Iterative Methods, second edition., SIAM, Philadelphia, PA, 1994.
[31] C.-H. Liu, D.Y.C. Leung, Parallel computation of atmospheric pollutant dispersion under unstably stratified atmosphere, Int. J. Numer. Methods Fluids 26 (1998) 677–696.
[32] C.-H. Liu, D.Y.C. Leung, Development of a finite element solution for the unsteady Navier–Stokes equations using projection method and fractional-θ-scheme, Comput. Methods Appl. Mech. Eng. 190 (2001) 4301–4317.
[33] C.-H. Liu, D.Y.C. Leung, C.-M. Woo, Development of a scalable finite element solution to the Navier–Stokes equations, Comput. Mech. 32 (2003) 185–198.
[34] C.-H. Liu, C.-M. Woo, D.Y.C. Leung, Performance analysis of a parallel finite element solution to the direct numerical simulation of fluid turbulence on Linux PC clusters, Appl. Math. Comput. 172 (2006) 731–743.
[35] C.-H. Liu, Turbulent plane Couette flow and scalar transport at low Reynolds number, J. Heat Transfer 125 (2003) 988–998.
[36] R. Nagaosa, Direct numerical simulation of vortex structures and turbulent scalar transfer across a free surface in a fully developed turbulence, Phys. Fluids 11 (1999) 1581–1595.
[37] S. Komori, R. Nagaosa, Y. Murakami, S. Chiba, K. Ishii, K. Kuwahara, Direct numerical simulation of three-dimensional open-channel flow with zero-shear gas–liquid interface, Phys. Fluids A 5 (1993) 115–125.
[38] S. Komori, H. Ueda, F. Ogino, T. Mizushina, Turbulence structure and transport mechanism at the free surface in an open channel flow, Int. J. Heat Mass Transfer 25 (1982) 513–521.
[39] S. Komori, Y. Murakami, H. Ueda, Relationship between surface renewal and bursting motions in an open-channel flow, J. Fluid Mech. 203 (1989) 103–123.
[40] S. Komori, R. Nagaosa, Y. Murakami, Mass transfer into a turbulent liquid across the zero-shear gas–liquid interface, AIChE J. 36 (1990) 957–960.
[41] G.A. Briggs, Analytical parameterization of diffusion: the convective boundary layer, J. Climate Appl. Meteor. 24 (1985) 1167–1186.
[42] L. van Haren, F.T.M. Nieuwstadt, The behavior of passive and buoyant plumes in a convective boundary layer as simulated with a large-eddy model, J. Appl. Meteor. 28 (1989) 818–832.